Macromolecules **1998,** *31,* 5861−5879

Discontinuous Molecular Dynamics Studies of End-Linked Polymer Networks

N. R. Kenkare, S. W. Smith, C. K. Hall,* and S. A. Khan

Department of Chemical Engineering, Box 7905, North Carolina State University,
Raleigh, North Carolina 27695-7905

Received February 2, 1998; Revised Manuscript Received May 22, 1998

ABSTRACT: Discontinuous molecular dynamics simulations are used to study the structure and relaxation of large, off-lattice, near-perfect, tri- and tetrafunctional polymer networks at a packing fraction of 0.43. The networks are constructed by end-linking freely jointed, tangent hard-sphere chains ranging in length from $N = 20$ to $N = 150$ and are then relaxed for 5−20 billion collisions. The simulation trajectories are used to calculate the radius of gyration and end-to-end distance of the network chains, the static structure factor of the cross-links, the mean-squared displacement of the cross-links and chain inner segments, the intermediate scattering function of the chains, and the elastic modulus of the network. The structure and properties of the networks are shown to depend heavily on the manner in which the network is initially constructed. The dynamics of the network cross-links and chain inner segments are similar to those of melt chains at short times and show evidence of spatial localization at long times. The results from the elastic moduli and long-time cross-link and chain displacement calculations indicate that entanglement constraints act in conjunction with cross-link constraints to reduce cross-link and chain mobility. The presence of entanglements appears to cause the magnitude of the elastic modulus to be larger than the affine/phantom model predictions.

Introduction

Cross-linked polymer systems (or networks) are industrially important materials that have wide applications in the manufacture of automobile tires, sealants, gaskets, coatings, and apparel. Although these systems have been studied for nearly a century, our understanding of their structure−property relationships is far from complete. This is due primarily to the complex nature of network relaxation processes and the variety of factors that affect them, including cross-link density, chain density, junction functionality, extent and nature of irregularities, and strand polydispersity.

The earliest molecular theories of rubberlike elasticity were the affine model of Wall[1] and Flory,[2] and the phantom model of James and Guth.[3] Both models apply to perfect monodisperse networks, although the phantom model can be extended to incorporate the effect of network irregularities in a qualitative manner.[4] The primary difference between these models arises from their treatment of junction motion. The affine model assumes that the network junctions are constrained by the presence of the surrounding chains to fixed locations relative to the rest of the network, so that they can only move affinely in response to a deformation of the network. In contrast, the phantom model assumes that the junctions are allowed to fluctuate freely about their mean positions, which, themselves, deform affinely with strain. The extent of junction fluctuation is invariant with strain. Neither model accounts for the excluded volume of the chains or for any “entanglement” effects. Both the affine and phantom models fail to predict the behavior of real networks over a range of deformations, as has been shown by uniaxial extension/compression and swelling experiments,[5−7] although the phantom model has been found to work in the large deformation limit, and the affine model in the low deformation limit. Junction motion in real networks falls between these two extremes; i.e., junction fluctuations are damped due to the dense packing of the chains but are not suppressed completely. The presence of excluded volume and entanglement constraints also restricts the configurational arrangements of the network chains.

The constrained junction model[8,9] was proposed to incorporate the damping effect of chain entanglements on the fluctuations of the junctions. In this model, the fluctuations of the junctions in a phantom domain (i.e., in a purely phantom network) are impeded by a constraint domain that represents the effect of the entanglements. The real mean position and average fluctuation of the cross-links in the constrained junction model are calculated by summing the contributions from both domains. As a result, the junctions of the network fluctuate but to a lesser degree than in the phantom model. Although the constrained junction model incorporates the effect of entanglement constraints only on the network junctions, and not on the chains, this model has been successful in qualitatively predicting the behavior of real networks including the deformation dependence of the reduced stress (the Mooney effect) and the maximums in the dilation modulus observed in swelling experiments.[6,7]

Several theories that incorporate the effect of topological constraints on network chains as well as on junctions have been presented, prominent among which are the slip-link models[10−15] and the tube models.[12,16−20] A variety of other approaches have been used including methods based on knot theory and topological invariance[21] and on replica theory as applied to random networks.[22] Since most of the above theories have been developed for perfect monodisperse networks, experimental validation of theoretical predictions using vulcanized or randomly cross-linked systems is not easy. Recently a number of researchers have synthesized model end-linked networks to test theoretical predictions (Mark et al.[23−25] Rennar and Opperman,[26] Patel et al.[27]) The advantage of using these networks is that

S0024-9297(98)00142-9 CCC: $15.00

the strand length distribution between cross-links is known since it is identical to that of the precursor melt, although the difficulty of obtaining a sufficiently monodisperse precursor system remains. Even for these “model” networks, however, it is difficult to obtain a precise knowledge of the extent of cross-linking of the system and the proportion of irregularities, such as dangling ends, loops, or free chains, which is necessary in order to investigate the structure−property relations of networks.

Computer simulations offer the unique opportunity to study the static and dynamic properties of polymer networks outside the laboratory and to test theoretical predictions. Since simulations offer the advantage of greater control over the cross-linking process than is feasible via experiments, as well as precise knowledge of the network structure, we can obtain an idea of the relative importance of the various factors that contribute to rubberlike elasticity. However, due to the necessity for large system sizes and long relaxation times, few simulation studies of network relaxation have been conducted. Early network simulations (Eichinger and co-workers,[28−30] Akgiray[31]) examined large static networks, i.e., networks in which the cross-linker and chains were not allowed to move during or after cross-linking. They focused primarily on the structure and composition of the formed networks. Subsequently, Gao and Weiner[32−34] conducted a set of molecular dynamics simulations of end-linked tetrafunctional networks, in which the chain ends were fixed on the vertices of a tetrahedral or cubic lattice and moved affinely with network deformation. They investigated the relative contributions of covalent bonding and of excluded volume to the microscopic stress under deformation.

The first simulations of the relaxation of continuous space networks were performed by Duering, Kremer and Grest, on randomly cross-linked[35,36] and end-linked systems.[37,38] The end-linked networks were constructed from equilibrated melts of linear chains by attaching a stoichiometric proportion of tetrafunctional cross-linkers to randomly chosen chain ends and allowing the cross-linkers to capture chain ends within a given reaction radius until the cross-linker became saturated. The beads interacted by a combination of the truncated Lennard-Jones and FENE potentials, and the system was relaxed using the Langevin integration technique. Duering et al.[38] calculated and analyzed the kinetics of end-linked network formation as well as the static and dynamic properties of large tetrafunctional networks (30 000−50 000 particles) with chain lengths 12, 20, 35, 50, and 100 at a number density of 0.85. They found that the mobility of the cross-links was far lower than that predicted by the phantom model except for the shortest chain length and that the plateau value of the cross-link displacement at long times agreed with the predictions of the localization model of Vilgis and Boue.[39,40] The chain inner segment mobility also showed qualitative agreement with a tube model-based prediction, and the tube diameters obtained from their analysis were consistent with the results of their simulations on the dynamics of melts.[41] They also introduced a method by which the time-dependent modulus of the network could be calculated from the autocorrelation of the Rouse modes of random walk chains constructed from the network, obviating the need for a computationally prohibitive stretching or shear experiment. The values of the time-dependent moduli were found to exceed those of both the phantom and affine models, suggesting an additional contribution to the modulus due to trapped entanglements, as proposed by Langley,[42] and Graessley and co-workers.[43,44] In addition to the Lennard-Jones networks, Duering et al. also studied a few phantomlike networks, in which the Lennard-Jones interaction between all beads except nearest neighbors or next-neighbors along the chains was switched off. The cross-link and inner segment displacements for these networks exhibited a scaling consistent with phantom network predictions.

Trautenberg et al.[45] conducted bond fluctuation studies of athermal end-linked tetrafunctional networks on a cubic lattice, using a network formation procedure similar to that used by Duering et al. The initial (un-cross-linked) system consisted of a melt of linear chains with tetrafunctional cross-linker particles added in stoichiometric proportion. The system was allowed to relax, and then the cross-linker molecules were allowed to react with nearest-neighbor chain ends with a probability that was chosen to model slow- or fast-cross-linking reactions. The dependence of the cross-linking kinetics on the reaction rate was analyzed. Recently Holz et al.[46] extended these studies to investigate the force−deformation relations during the uniaxial extension of networks. The force−deformation relations were found to lie between the affine and the phantom predictions.

Attempts to simulate the relaxation of continuous-space network systems using standard Monte Carlo methods are relatively rare due to the necessity for system-specific Monte Carlo moves to keep the network structure intact during relaxation. Escobedo and de Pablo[47−49] used special ECCB, “slab” and “cluster” moves in their studies of the PVT and swelling behavior of tetrafunctional diamond networks and proposed a new theoretical approach to gel swelling.[49]

In this work, we present a study of the structure and relaxation of end-linked trifunctional networks in which we apply the discontinuous molecular dynamics (DMD) technique to the hard-chain model, the simplest possible continuous-space molecular model of a polymer chain. The network is cross-linked from a melt of linear chains without the use of explicit cross-linker molecules. Each chain end is allowed to attach to any other chain end that it collides with in the course of the simulation, up to a maximum of two other chain ends in a trifunctional network or three other chain ends in a tetrafunctional network. This cross-linking process is carried out at a low packing fraction (e.g., $\phi = 0.3$) due to the difficulty of achieving near-complete cross-link formation at high densities, especially for long-chain-length networks. After the network is formed, the packing fraction is increased to reach a final value of $\phi = 0.43$. We studied trifunctional end-linked networks of chain lengths 20, 35, 50, 100, and 150 and one tetrafunctional network of chain length 100, all at a volume fraction of 0.43, and over time scales of 4.5 orders of magnitude (5−20 billion collisions/state point), in order to be able to access the long-time relaxation region. Because cross-linked systems have quenched disorder, the system sizes for all of the above simulations were large, and each system contained between 21 000 and 45 000 particles. This also allowed us to obtain sufficient averaging for the cross-link properties.

Although our work was initially motivated in part by our desire to compare our results for trifunctional hard-chain networks with the tetrafunctional truncated Lennard-Jones networks of Duering et al. and hence to learn how functionality influences network relaxation, the most intriguing consequence of this comparison was that the properties depend strongly on the manner and density at which cross-linking is carried out. As described above, we cross-linked our networks at a low density and then increased the packing fraction. It appears that our method of cross-linking results in the formation of networks with lower end-to-end chain distances, and possibly a different topology with respect to trapped entanglements, than if the cross-linking had been carried out at the high packing fraction finally desired. In contrast, Duering et al. cross-linked their networks for the most part at packing fractions close to or equal to the final packing fraction of the cross-linked network. They also used a supplementary techinque to achieve a near-complete extent of cross-linking (described in detail under Chain Dimensions) that resulted in their network chains having somewhat larger end-to-end distances than melt chains at the same densities. We can draw a parallel to experimental systems by considering that a network that is initially cross-linked at a low density is analogous to a solution-cured network from which the solvent is subsequently extracted, while a network that is cross-linked at high density is analogous to a bulk-cured network. The method of cross-linking has been shown[5,50−52] to result in qualitative differences between the elastic response of solution-cured networks and bulk-cured networks. The properties of networks thus depend both on the "preparative ensemble" and the "final ensemble",[53] in contrast to chain systems where the preparative ensemble does not influence the properties of the final system. To probe the relation between the preparation and the structure and properties of the network, we carried out a test study of two small 100-mer trifunctional networks initially cross-linked at low and high packing fractions ($\phi = 0.15$ and 0.43, respectively). The test networks were both relaxed at a packing fraction of 0.43. The dynamics of the networks showed distinct differences, which can only be related to their cross-linking densities and which confirm the dependence of network properties on the method of network preparation.

We investigated the relaxation of the large trifunctional networks described earlier with a view to assessing the relative importance of cross-link and entanglement constraints on junction and chain dynamics and on elastic moduli. Our results at short times show that the cross-link and chain displacements and the chain-scattering function are time-dependent and behave in a manner that is consistent with the Rouse model predictions. Our results at long times show that the cross-link and chain displacements and chain-scattering function reach a time-independent plateau reflecting the localization of the chains and junctions. Both these results confirm similar findings by Duering et al. The magnitudes of our long-time cross-link and chain displacement plateaus are, however, much larger than those found by Duering et al., partly because of the difference in network functionality and partly because of the different network preparation methods used. On comparing our long-time cross-link and chain displacement plateau results with the predictions of various network entanglement theories, we find that the data show qualitative agreement with the tube-based models of network dynamics, although the quantitive agreement is not good. In contrast, Duering et al. concluded that their long-time displacement data agreed very well qualitatively and quantitatively with the predictions of the tube-based network models. The elastic moduli from our simulations exceed both the phantom and affine model predictions and support Langley's[42] and Graessley's[43,44] suggestion that there is an entanglement contribution to the network elastic properties in addition to the cross-linking contribution. The magnitude of the entanglement contribution (i.e., the difference between the simulation moduli and the affine/phantom moduli) increases with chain length as expected. These observations from the elastic moduli calculations are in agreement with the results of Duering et al. as well as with recent experiments.[26,27]

This paper is organized as follows: the sections present, in order, the molecular model and the simulation technique; the cross-linking technique; analyses of the static properties of the formed networks; the dynamics of network relaxation; the elastic properties of the networks, and a summary of our conclusions.

Molecular Model and Simulation Technique

The basic unit of a network is a single polymer molecule, which is represented in this study by a freely jointed chain of tangent hard spheres (beads), the so-called hard-chain or pearl necklace model. The chain is flexible; i.e., the bond angle between successive beads can take on any value that does not cause overlap along the chain. This molecular model incorporates two of the basic attributes of polymer chain architecture—connectivity and excluded volume. The potential energy of interaction between any two beads on the same or neighboring chains is given by

$$\begin{aligned} U(r) &= 0, \quad r > \sigma \\ &= \infty, \quad r \le \sigma \end{aligned} \tag{1}$$

where σ is the bead diameter.

The molecular dynamics treatment of the hard-chain model is difficult due to the tangency constraint and the flexibility requirement. To overcome this problem, Rapaport[54,55] suggested an elegant approach in which the bond length l is no longer kept constant at $l = \sigma$ but is allowed to vary freely over a range between σ and $\sigma(1 + \delta)$, where δ is very small. Thus, the chain effectively becomes a collection of hard spheres connected to each other by sliding links. As $\delta \rightarrow 0$, the chain approximates the tangent hard-sphere chain model. Our simulations use a further modification of the tangent hard-sphere model suggested by Bellemans et al.[56] in which the bond length varies between $\sigma(1 - \delta)$ and $\sigma(1 + \delta)$, so that the average bond length is close to σ, and the chain effectively mimics the tangent hard-sphere chain.

The advantage of allowing the bond length to vary, as in the Rapaport and Bellemans algorithms, is that the trajectories of the chain segments can be partially decoupled, resulting in linear trajectories between collisions. The system dynamics can then be treated by the discontinuous molecular dynamics techniques developed by Alder and Wainwright[57−59] for hard-sphere systems. The only difference is the addition of a bond stretch event, which is treated in the same way as one treats a particle trapped in an infinitely deep square well of width $\sigma(1 + \delta)$.[60]

The system evolves on a collision-by-collision basis by locating the next event (a core collision or a bond stretch), advancing all the segments until that event occurs, calculating collision dynamics for the colliding pair of segments, and then repeating this process. The sequence of events is determined from the set of collision times in the system. At each step of the simulation, the colliding segments undergo an event in which their velocities change in both magnitude and direction. Since new collision times and partners for the colliding segments must be calculated after each event, the calculation of collision times is the most expensive part of a discontinuous molecular dynamics simulation.

We have used a number of efficiency techniques to reduce the computational effort involved in relaxing large-particle systems over long times. Our molecular dynamics algorithm (originally developed for linear hard-sphere chains[61]) is based on single-event scheduling and yields 18−20 million collisions per CPU hour on an Alpha 366MHz workstation when simulating 21 000−45 000 segment network systems. Neighbor lists are employed to restrict the search for collision partners to a small area around a given segment. Linked lists are used to avoid unnecessary reconstruction of neighbor lists, and a simple binary tree is used to schedule events. The false positioning technique is incorporated so that particle positions are updated only at discrete time intervals and not at every collision. A comprehensive description of the use of the above efficiency techniques in the discontinuous molecular dynamics algorithm is given in the paper by Smith et al.[61]

All of the simulations were conducted in a cubical simulation cell with periodic boundary conditions. The bond stretch parameter δ was set to 0.1, since this allows sufficient displacement of the particles, while closely approximating the tangent hard-sphere model and preventing bond crossing. The simulation times are presented throughout in terms of reduced units,

$$t^* = \left(\frac{k_B T}{m\sigma^2}\right)^{1/2} t \tag{2}$$

where m is the mass of a segment or particle.

Network Formation

We constructed five trifunctional networks containing 1200 chains of 20-mers, 600 chains of 35-mers, 450 chains of 50-mers, 225 chains of 100-mers, and 300 chains of 150-mers, respectively, as well as a tetrafunctional network of 300 chains of length 100, all at a volume fraction of 0.43. The volume fraction is defined as

$$\phi = \frac{\pi}{6}\frac{N_c N\sigma^3}{V} \tag{3}$$

where N_c is the number of chains in the network, N is the chain length, and V is the volume of the system.

Our objective was to construct nearly "perfect" networks, i.e., networks that contain very low percentages of dangling chains, loops, and free chains, since the presence of these irregularities significantly affects the elastic properties of the network. The starting point for network formation was a melt of linear chains. Due to the difficulty of achieving a high extent of cross-link formation at large packing fractions, the melts were grown and relaxed at packing fractions between 0.25 and 0.3 (lower than the required value of 0.43), using the technique of Smith et al.[61,62] The networks were then cross-linked from the melt, and finally the system volume fraction was increased to 0.43 by growing the segment diameter.[61,62]

Table 1. Network Structure[a]

N	x_{elastic}	$\bar{f}$	N_3	N_4	N_2	N_{end}	N_{loop}
20	0.95	2.99	796 (99.5)		3	6	49
35	0.95	2.99	395 (98.8)		3	9	18
50	0.95	2.99	296 (98.6)		2	8	13
100	0.88	2.97	143 (95.3)		5	11	5
150	0.83	2.94	185 (92.5)		11	23	8
100_{tetra}	0.96	3.80	31	125 (98.8)	2	3	5

[a] Network structure is reported for each system of chain length N, in terms of the elastically active fraction, x_{elastic}, average functionality of junctions, $\bar{f}$, number of saturated trifunctional and tetrafunctional junctions, N_3 and N_4 (the numbers in parentheses represent the percentage of saturated junctions), number of "bifunctional" junctions, N_2, number of free ends, N_{end}, and number of loops, N_{loop}.

The cross-linking took place by allowing bond formation between the chain ends as they collided with each other in the course of the simulation. Once a given chain end was bonded to two or three other chain ends (depending on whether the network was trifunctional or tetrafunctional), it became "saturated" and was not allowed to participate in further bond formation. A chain end that was bonded to more than one other chain end was considered to be a cross-link or junction of the network. Using this end-linking procedure, junction formation proceeded rapidly until ~90% of the chain ends were connected to at least one other chain end. After this point, there was a distinct slowing down in the rate of cross-linking. At this stage, the network contained a significant number of dangling ends and long chains associated with unsaturated bond formation (resulting in "bifunctional" junctions). To force the formation of more saturated junctions, we modified the algorithm to allow further bond formation only between existing bifunctional junctions and the remaining unreacted chain ends. When no further saturated junction formation took place (because the distance between the remaining bifunctional junctions and unreacted chain ends was too large), we broke up the bifunctional junctions and allowed the network (now containing only saturated or dangling chain ends) to relax for ~50 million collisions, so that the dangling chain ends were sufficiently displaced, before allowing bond formation again. By this process, the network formation continued until fewer than 5% of the remaining chains in the network were dangling, and 96−99% of the chain ends were participating in saturated junctions. At this stage, we stopped the network formation process, since any further bond formation took place extremely slowly and did not appreciably change the network structure. The volume fraction of the network was then increased to the required value of 0.43 by growing the segment diameter,[61,62] and the system was allowed to relax.

Since the elastic properties of cross-linked structures are dependent on the extent of cross-linking, and on the proportion of dangling chains, loops, and other defects, it is essential to calculate these quantities for the above networks. Table 1 displays the following measures of the structural completeness of the network: the elastically active fraction, x_{elastic}, the average functionality of the junctions, $\bar{f}$, the number of trifunctional junctions,

N_3, the number of tetrafunctional junctions, N_4, the number of bifunctional (unsaturated) junctions, N_2, and the number of dangling ends and loops, N_{end} and N_{loop}. Perhaps the most important measure of the "perfectness" of our networks is the elastically active fraction, x_{elastic}, which is defined to be the fraction of the chains that are connected at both ends to junctions with at least three independent paths to the network.[63,64] The elastically active fraction is calculated in the table by subtracting the number of unsaturated junctions, dangling chains, and loops from the total number of network chains; it lies between 0.92 and 0.96 for all the networks considered. The average functionality of the junctions, $\bar{f}$, is close to the ideal value of 3 for the trifunctional networks and is close to 4 for the tetrafunctional network. None of the networks have any free chains. Due to the high elastic fraction, and the low number of network irregularities, these systems can be considered to be nearly perfect networks.

The data in Table 1 is not sufficient to deduce whether the networks consist of a single large cross-linked structure spanning the simulation cell or of a large primary network and several smaller, secondary, interpenetrated treelike structures that are unconnected to the primary network. This was checked using the following algorithm: a "walk" was conducted, starting from a randomly chosen chain end and then proceeding along the network chains, making a random choice of direction at every cross-link encountered, until it ended in a loop or a dangling end. All the chains encountered along this path obviously belonged to the same network structure as the originally chosen chain end. Then we picked another chain end that was part of the previous walk and repeated the process several times, until most or all the chain ends had been encountered. After several iterations, the number of chain ends that were encountered remaned constant, and we considered the search to be complete for that network structure. The connectivity of all other network or treelike structures was similarly checked. We found that our networks consisted of one large cross-linked structure composed of nearly all the chains in the system. The sol fraction, defined as the fraction of chains that are not attached to the large network structure, was negligible (1.17% for the 20-mer network and zero for all the other networks). The chains comprising the sol fraction were not included in the calculation of static and dynamic properties.

During the cross-linking process, we kept track of the elastic fraction, x_{elastic}, and the fraction of chain ends, $N_{\mathrm{sat}}/2N_{\mathrm{c}}$, that participated in saturated junctions, both of which increased with time as the cross-linking proceeded. Figure 1 shows the elastic fraction and the fraction of saturated chain ends as a function of cross-linking time. These data were collected only during the initial cross-linking process, i.e., before the algorithm modifications described previously were applied and before the packing fraction was increased to its final value. From Figure 1, both the elastic fraction and the number of saturated chain ends increase rapidly with time until a little over 90% of the chain ends are cross-linked. At this stage, due to the reduced mobility of the remaining chain ends (most of which are attached to the network at at least one end), the network formation slows down dramatically.

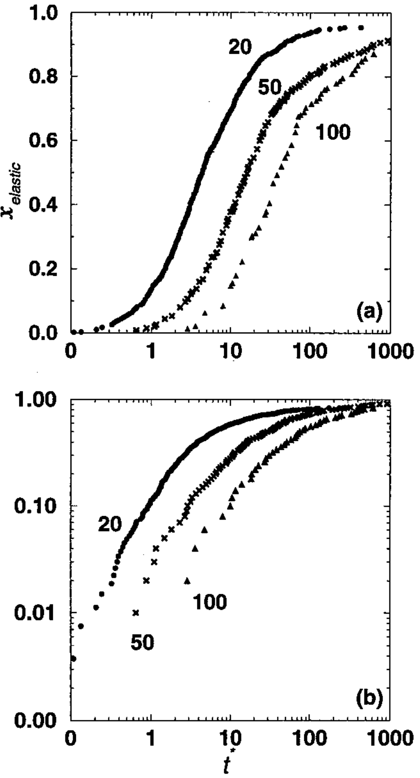

Figure 1. (a) Elastic fraction, x_{elastic}, and (b) fraction of saturated chain ends, $N_{\mathrm{sat}}/2N_{\mathrm{c}}$, as a function of reduced time, t^*, during network formation.

Table 2. Sizes of the Simulated Systems[a]

chain length N	no. of chains N_{c}	cross-linking density ϕ_{ini}	simulation cell length $L\sigma^{-1}$	billions of events	simulated time $t^*_{\mathrm{total}} \times 10^{-3}$
20	1200	0.3	30.8	4.0	14.0
35	600	0.3	29.46	8.5	34.1
50	450	0.26	30.15	10.0	37.5
100	225	0.26	30.15	14.2	53.2
150	300	0.15	37.98	16.5	30.9
100_{tetra}	300	0.15	33.18	10.0	28.1

[a] The sizes of the simulated systems are given in terms of the chain length N and number of chains N_{c}. Other simulation parameters include the initial cross-linking density, ϕ_{ini}, the simulation cell length, $L\sigma^{-1}$, the number of collisions reported in billions of events, and the total reduced simulation time for each network studied.

Network Properties

After the cross-linking was stopped, the networks were allowed to relax for 5−20 billion collisions each, and stored trajectories were used to calculate static and dynamic properties. Due to the large system size and the slow relaxation, only one run was conducted for each case. The system sizes and total run lengths, along with the initial cross-linking densities and simulation cell lengths, are summarized in Table 2. The networks' static properties were investigated by calculating the mean-squared end-to-end distance and mean-squared radius of gyration of the network chains, and the static coherent scattering function of the cross-links. The networks' dynamic properties were investigated by calculating the mean-squared displacement of the cross-links and inner chain segments, the intermediate scattering function, and the elastic modulus.

Since single runs were conducted in all cases, uncertainties in the chain dimensions (mean-squared end-

Table 3. Static Properties of Networks[a]

N	$\langle R^2\rangle/\sigma^2$	$\langle R_G^2\rangle/\sigma^2$	$\langle R^2\rangle/\langle R_G^2\rangle$	Z
20	28.39 (±0.03)	4.71 (±0.01)	6.03	98.98
35	54.14 (±0.38)	8.94 (±0.03)	6.06	174.14
50	71.67 (±0.52)	12.29 (±0.10)	5.83	249.36
100	159.36 (±2.8)	25.77 (±0.39)	6.18	499.77
150	189.83 (±2.09)	34.62 (±0.06)	5.48	750.91
100_{tetra}	143.53 (±1.88)	23.64 (±0.27)	6.07	499.52

[a] Mean-squared end-to-end distance $\langle R^2\rangle/\sigma^2$, mean-square radius of gyration $\langle R_G^2\rangle/\sigma^2$, ratio of $\langle R^2\rangle$ and $\langle R_G^2\rangle$, and compressibility factor Z. Values in parentheses show the standard deviation in $\langle R^2\rangle/\sigma^2$ and $\langle R_G^2\rangle/\sigma^2$. Standard deviation in Z is less than 0.01%.

to-end distances and mean-squared radii of gyration) and in the compressibility factors were obtained by dividing the long runs into three or more subruns and calculating the standard deviation thereof. Uncertainties in the long-time asymptotic values of the cross-link and segment displacements, intermediate scattering function, and elastic modulus were estimated by using a linear regression fit in the plateau region of the data.

Static Properties. (1) Chain Dimensions. Most network theories (e.g., the affine, phantom, and constrained junction models) assume that the network chains follow Gaussian statistics, since the network is constructed by cross-linking a melt of Gaussian chains. However, it is conceivable that chain dimensions could be altered during cross-linking. For instance, our procedure of cross-linking the melt at an initial low density and then growing it to the final required density could have affected the chain dimensions and possibly their Gaussian characteristics. We therefore calculated the network chain dimensions in order to check whether the network chains obeyed Gaussian statistics after cross-linking.

The mean-squared network chain end-to-end distance $\langle R^2\rangle$, the mean-squared radius of gyration $\langle R_G^2\rangle$, and the compressibility factor Z, were calculated for all network systems and reported in Table 3. The compressibility factors were calculated using the Clausius virial theorem in the following form:

$$Z = N - \frac{m\sum_{\text{coll}} \mathbf{r}_{ij}\cdot\Delta\mathbf{v}_{\text{ij}}}{3\ N_c k_B T t_e} \tag{4}$$

where t_e is the elapsed simulation time over which the sum is calculated, k_B is the Boltzmann constant, T is the temperature, m is the mass of a segment, $\mathbf{r}_{ij}$ is the vector between segment centers at a collision, and $\Delta\mathbf{v}_{ij}$ is the velocity change for the colliding pair. Figure 2 presents $\langle R^2\rangle/\sigma^2$ and $\langle R_G^2\rangle/\sigma^2$ as a function of chain length N. The asterisks represent the chain dimensions for the 100-mer tetrafunctional network. Both the mean-squared end-to-end distance and the mean-squared radius of gyration of the network chains scale linearly with chain length such that the ratio $\langle R^2\rangle/\langle R_G^2\rangle \approx 6$, although the chains in the 150-mer network are somewhat contracted compared to the other networks. For a Gaussian chain, the mean squared end-to-end distance should satisfy the relation

$$\langle R^2\rangle = l_2 l_p^2 (N - 1) \tag{5}$$

where l is the bond length and l_p is the persistence length, which is a measure of chain stiffness. A linear regression fit to the $\langle R^2\rangle$ data shows that our network chains satisfy the above relation and that their mean-squared end-to-end distance has the form $\langle R^2\rangle = 1.3(N - 1)$. Thus, the characteristic dimensions of the Bellemans chains in the endlinked networks follow Gaussian statistics. The regression fit to the $\langle R^2\rangle$ data also allows us to obtain the persistence length of the network chains, $l_p = 1.14 \pm 0.05$. The averge bond length $l \approx 1$.

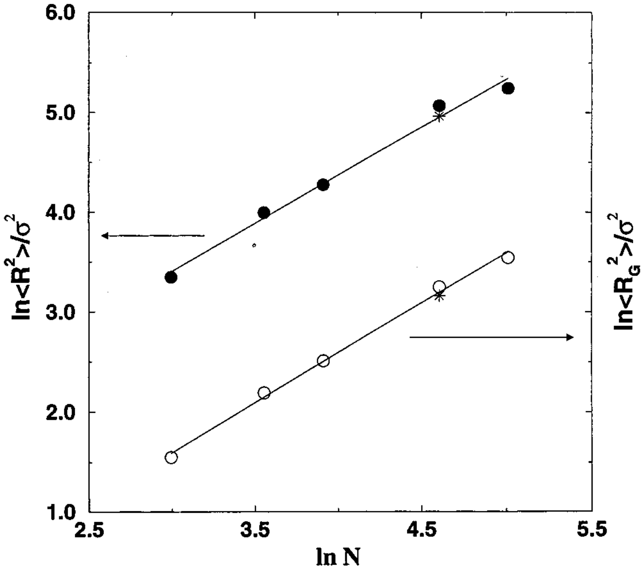

Figure 2. Mean-squared end-to-end distance, $\langle R^2\rangle/\sigma^2$, and radius of gyration, $\langle R_G^2\rangle/\sigma^2$, for trifunctional networks of strand length 20, 35, 50, 100, and 150, and for a tetrafunctional network of chain length 100 (indicated by asterisks). The error bars are smaller than the symbols size.

The network chain dimensions in our studies are somewhat smaller than the chain dimensions in a hard-chain melt at similar packing fractions (by comparison with the work of Smith et al.[62]) as shown in Figure 3a. In contrast, the network chain dimensions in the study by Duering et al. are larger than the chain dimensions in the corresponding melts,[41] as shown in Figure 3b. This is a result of the different cross-linking techniques used.

In our method, cross-linking takes place whenever an unsaturated chain end collides with another unsaturated chain end. Because there are no conditions imposed on the cross-linking (i.e., no explicit cross-linker molecules), a chain end is likely to attach to the chain end nearest it in space, thus having little effect on the chain dimensions. On the other hand, since the cross-linking is carried out at a low density ($\phi \le 0.3$) and the networks are subsequently grown to a high density ($\phi = 0.43$), the network chains are somewhat collapsed relative to melt chains at the same density, as shown in Figure 3a. To understand why network chains effectively collapse when the packing fraction is increased, it is helpful to first consider the opposite case, i.e., a network cross-linked at a high packing fraction, say ϕ_{initial}, for which the packing fraction is subsequently decreased to ϕ_{final}, where $\phi_{\text{initial}} > \phi_{\text{final}}$. At the density of cross-linking, ϕ_{initial}, the network chains have average random configurations appropriate to that density. When the density of the system is decreased to ϕ_{final}, the chains are stretched because their ends are connected to the rest of the network structure, and they cannot attain the corresponding melt configurations. Thus, at the low packing fraction, ϕ_{final}, the network chains are somewhat extended relative to melt chains

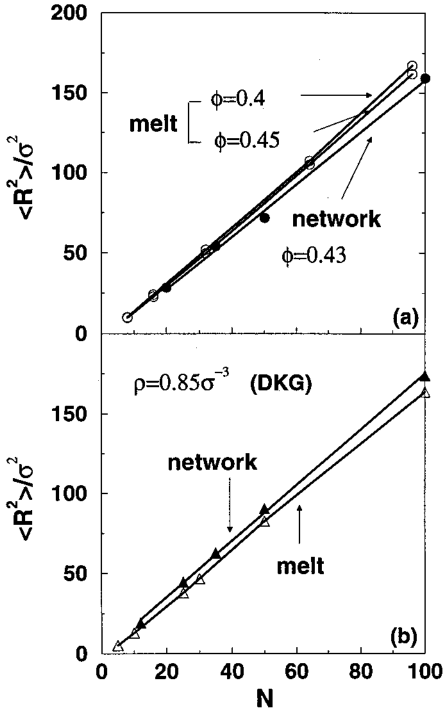

Figure 3. Comparison of the mean-squared end-to-end distances, $\langle R^2\rangle/\sigma^2$, in melts and networks. Filled symbols indicate network data and open symbols indicate melt data: (a) hard-sphere chain trifunctional networks (simulation results) and hard-sphere chain melts (results from ref 62) and (b) truncated Lennard-Jones networks (results from ref 38) and melts (results from ref 41).

at the same density. Applying the same reasoning for the case of $\phi_{\text{initial}} < \phi_{\text{final}}$, i.e., for a network that is cross-linked at a low density and then grown to a higher density, we expect the high-density network chains to be somewhat collapsed compared to melt chains at the higher density.

From an experimental point of view, our cross-linking technique is equivalent to a procedure in which cross-linking is done in solution, and the solvent is subsequently extracted from the system, resulting in somewhat collapsed chains,[5,50,65] relative to a network formed by curing a bulk melt. It is the converse of a process described by Ferry[65] in which a network formed by curing a bulk melt and then swelled in a solvent contains somewhat extended chains relative to a network that is cross-linked in solution at the same density.

Another possible consequence of our cross-linking at low packing fractions is the occurrence of fewer interchain contacts during the cross-linking[5,50] and, hence, fewer entanglements or "knots" in the system. This topology, created during cross-linking, remains "frozen" in the system and hence impacts the network dynamics.

The cross-linking technique used by Duering et al. involves searching for free chain ends within a certain reaction radius (1.3σ) of an unsaturated cross-linker. In order to decrease the number of free ends and unsaturated cross-links in the system after the initial cross-linking, by Duering et al. increased the reaction radius to 4σ and slightly lowered the density of the system (from a number density of 0.85 to 0.75). The large cross-linker bond lengths formed due to the expanded reaction radius were then allowed to shrink to the regular system bond length as the system relaxed. Once the cross-linking was done, the system number density was again increased to 0.85. This technique of considerably increasing the reaction radius in order to speed up network formation results in the chain being somewhat extended relative to the melt as shown in Figure 3b.

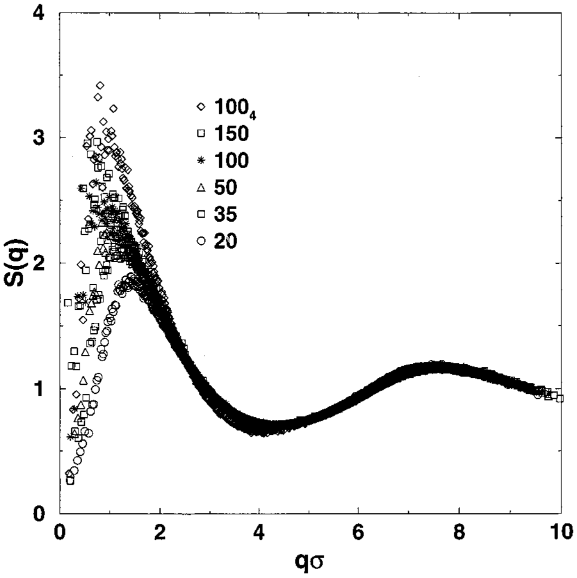

Figure 4. Static structure factors, $S(\mathbf{q})$ of the cross-links of the trifunctional networks versus the wave vector, $\mathbf{q}\sigma$, for all chain lengths.

(2) Static Structure Factor of the Cross-Links. An important quantity in studying network structure is the cross-link static structure factor, which gives us information about the spatial distribution of the junctions in the network. The cross-link static structure factor, $S_x(\mathbf{q})$, is defined[66] as

$$S_x(\mathbf{q}) = \frac{1}{N_a}\sum_{n,m}^{N_a}\langle \exp[i\mathbf{q}(\mathbf{r}_n - \mathbf{r}_m)]\rangle \tag{6}$$

where $\mathbf{q}$ is the scattering vector, N_a is the number of chain ends that are part of the elastically active network, and $(\mathbf{r}_n - \mathbf{r}_m)$ is the vector between any pair of chain ends, n and m. In order to minimize size effects, the scattering vectors $\mathbf{q}$ are chosen such that their magnitudes are multiples of the box length, i.e.,

$$|\mathbf{q}| = \frac{2\pi}{L}\{q_x, q_y, q_z\} \tag{7}$$

where q_x, q_y, q_z can take on any integer values such that their sum is greater than zero. Essentially, $S_x(\mathbf{q})$ is the spatial Fourier transform of the radial distribution function of the cross-links and is thus a measure of the variations of the local cross-link density in the simulation cell.

Figure 4 shows the static structure factor $S_x(\mathbf{q})$ versus the wave vector $\mathbf{q}\sigma$ for all the networks. The first peak at low $\mathbf{q}\sigma$ is of importance to us, since the corresponding wavevector $\mathbf{q}_{\max}$ can be used to calculate the average distance between cross-links, from the relation $r_x^{\text{av}} = 2\pi/|\mathbf{q}_{\max}|$. The values of r_x^{av} estimated from the structure factor peaks in Figure 4 are shown in Table 4. Due to the scatter in the $S_x(\mathbf{q})$ curves, particularly at longer chain lengths, these values of $\mathbf{q}_{\max}$ were obtained from the graph by using a regression fit to the curves. The average inter-cross-link distance increases with chain length as expected and is much smaller than the square root of the mean-squared end-to-end distance of the

Table 4. Simulation Results[a]

N	r_x^{av}/σ	N_x^{av}	$g_x(t\rightarrow\infty)/\sigma^2$	$\langle(\Delta R)^2\rangle_{ph}/\sigma^2$	$g(t\rightarrow\infty)/\sigma^2$
20	4.45	1.72	18.85 (0.42)	18.93	25.2 (0.73)
35	5.10	3.00	24.2 (0.51)	36.9	32.8 (1.09)
50	5.84	3.04	30.5 (1.41)	47.8	42.5 (1.72)
100	6.81	6.38	29.8 (1.2)	106.82	47.44 (0.97)
150	7.67	5.79	40.0 (2.07)	126.55	55.5 (2.03)
100_{tetra}	6.82	5.43	30.0 (0.27)	53.83	51.56 (1.86)

[a] Simulation results for the average distance between cross-links, r_x^{av}/σ, the average number of cross-links in the volume occupied by a network chain, N_x^{av}, the asymptotic mean-squared displacement of the cross-links, $g_x(t\rightarrow\infty)/\sigma^2$, the phantom theory prediction for the cross-link displacement variance, $\langle(\Delta R)^2\rangle_{ph}/\sigma^2$, and the inner monomers along the chains $g(t\rightarrow\infty)/\sigma^2$. Values in parentheses give the standard deviation in $g_x(t\rightarrow\infty)/\sigma^2$ and $g(t\rightarrow\infty)/\sigma^2$.

chains (see Table 3), except for the shortest chain length, $N = 20$. The fact that the average inter-cross-link distance is smaller than the average end-to-end distance of the chains indicates that the networks are interpenetrated, i.e., that the space occupied by a network chain is also occupied by several other chains, and implies that entanglement effects are of significance in examining network relaxation.

Since knowledge of the extent of interpenetration of the network chains is useful in interpreting cross-link and chain dynamics, we employ our simulation results to calculate a measure of chain interpenetration suggested by Flory.[67] The *degree of interpenetration*, N_x^{av}, is defined as the average number of cross-links contained in the volume occupied by a network chain,[67]

$$N_x^{av} = \langle R^2\rangle^{3/2}(N_x/V) \tag{8}$$

where N_x is the number of cross-links in the network. Combining eq 3 (assuming ϕ to be constant) with the relation, $N_x = 2N_c/f$, where N_c is the number of chains, the above relation can be expressed for a perfect end-linked network, as

$$N_x^{av} \propto \langle R^2\rangle^{3/2}/Nf \tag{9}$$

Thus, the degree of interpenetration scales inversely with network functionality and proportionally with the square root of the chain length (since $\langle R^2\rangle \propto N$, for Gaussian chains). Equation 8 and eq 9 assume that the cross-links are uniformly distributed over the simulation cell. Without such an assumption, the degree of interpenetration can be expressed in terms of the average distance between cross-links,[38] as

$$N_x^{av} = [\langle R^2\rangle^{3/2}/r_x^{av3}] \tag{10}$$

The above equation and eq 8 are equivalent if $r_x^{av3} = V/N_x$.

The simulation results for N_x^{av} calculated using eq 10, are displayed in Table 4 and show that, for trifunctional networks, the number of cross-links per chain volume increases with chain length, the exception being the 150-mer network. The N_x^{av} value for the 100-mer trifunctional network is greater than that for the 100-mer tetrafunctional network, in keeping with eq 9. Apart from the different functionalities of the networks, an additional contribution to the disparity in N_x^{av} between the 100-mer tri- and tetrafunctional networks comes from the fact that the tetrafunctional network was initially cross-linked at a lower density ($\phi_{ini}^{tetra} = 0.15$, from Table 2), than the trifunctional one ($\phi_{ini}^{tri} = 0.26$). The surprisingly low degree of interpenetration of the 150-mer trifunctional network is also related to its low initial cross-linking density ($\phi_{ini} = 0.15$), which is lower than that for the other trifunctional networks (Table 2).

We find that the number of cross-links per chain volume in our networks is much lower than those in the networks simulated by Duering et al. For example, our 100-mer tetrafunctional network has approximately 5.4 cross-links per chain volume compared to 9.55 cross-links for the 100-mer tetrafunctional network of Duering et al., indicating that the degree of interpenetration in their networks is much higher than in ours. In fact, even our trifunctional networks have a lower degree of interpenetration than the Duering et al. networks; our 100-mer trifunctional network has only 6.4 cross-links per chain volume while their tetrafunctional network has 9.55. We think that the cause of the structural difference between the networks of Duering et al. and ours again lies in the dissimilarity in cross-linking techniques. Since our networks are constructed at a lower packing fraction, there are fewer chain entanglements (trapped or otherwise) in the system and, hence, fewer cross-links (or chains) in the volume spanned by a given chain. This results in the degree of interpenetration being lower than if the cross-linking had been done at a high packing fraction. The low degree of interpenetration in our networks is also related to the fact that the somewhat collapsed chains in our networks sweep out a smaller volume[68] than the slightly expanded chains in the Duering et al. networks and, hence, encounter fewer spatially neighboring cross-links.

We would expect the dynamic properties of our networks, notably the mean-squared displacement of the inner segments and cross-links to reflect the disparity in the degree of interpenetration and, therefore, show higher values than the Duering et al. study. This is precisely what we will show under Mean-Squared Displacement of the Cross-Links.

Dynamic Properties

Information about the dynamics of dense polymeric systems can be obtained from the time-dependent displacement of the chain segments (and cross-links) and the dynamic scattering function. Valuable insights into the relaxation of cross-linked systems can be obtained by comparing the long-time behavior of the network mean-squared displacement and scattering functions with the long-time behavior of melts. Since most analyses of network relaxation are based[38,39,69] on the Rouse and tube model predictions of melt dynamics, we will first briefly summarize their highlights.

The Rouse model describes the dynamics of short-chain melts. The chain motion is treated by solving a linear Langevin equation to obtain the positions of the chain segments as a function of time. The fluid surrounding the chain is represented by a stochastic background that relaxes rapidly. Excluded-volume and hydrodynamic interactions are not taken into account, and the dynamics are primarily governed by localized interactions along the chain. The Rouse model predicts a specific time-dependent scaling behavior for the mean-squared displacement of the chain segments, $g(t)$, defined to be

$$g(t) \equiv \frac{1}{N}\sum_{i=1}^{N}\langle|r_i(t+t_0)-r_i(t_0)|^2\rangle \tag{11}$$

where the sum is over all chain segments i, and the ensemble average is over all time origins, t_0, and over all chains. The Rouse time τ_R, is defined to be the longest relaxation time of the chain end-to-end vector correlation function, and is given by

$$\tau_R \sim \zeta N^2/k_BT \tag{12}$$

where ζ is the friction factor. At times $t < \tau_R$, the motion of a chain segment is slowed down because of chain connectivity, and the mean-squared displacement scales with time as $g \sim t^{1/2}$. At times greater than the Rouse time, the chain is internally relaxed and diffuses freely, with $g(t) \sim t$.

The tube model describes the effect of topological interactions on the relaxation of long, entangled polymer chains and was developed by Doi and Edwards[70] within the framework of reptation theory. In this model, the fluid surrounding a melt chain relaxes much more slowly than the chain itself, confining the chain to a tubelike region about its primitive path. The tube model predicts that the motion of a single chain is characterized by four distinct time regimes during which the segment mean-squared displacement, $g(t)$, displays the following scaling behavior with time: (1) $g \sim t^{1/2}$ until $t = \tau_E$, where τ_E, the entanglement time, is the time it takes for a chain to discover its confinement to a tube in the lateral direction; (2) $g \sim t^{1/4}$ for $\tau_E < t < \tau_R$, where τ_R is the Rouse time; (3) $g \sim t^{1/2}$ for $\tau_R < t < \tau_D$, where τ_D, the disengagement time, is the time it takes for the chain to "disengage" from the tube; and (4) $g \sim t$ for $t > \tau_D$, the so-called free diffusion limit.

(1) Mean-Squared Displacement of the Cross-Links. Panels a and b of Figure 5 present the reduced cross-link mean-squared displacement, $g_x(t)/\sigma^2$, versus reduced time, t^*, on linear and natural log scales, respectively, the latter being useful for deducing the scaling with time. The cross-link mean-squared displacement is calculated as

$$g_x(t) \equiv \frac{1}{N_a}\sum_{i=1}^{N_a}\langle|r_i(t+t_0)-r_i(t_0)|^2\rangle \tag{13}$$

where N_a is the number of elastically active chain ends. The averaging is done over all time origins, t_0, and over all chain ends, i, in the elastically active cluster.

The curves in Figure 5b show an initial slope of ~0.5 that is in agreement with the Rouse model prediction and reflects the effect of chain connectivity. After the initial $t^{1/2}$ scaling region, the slope decreases continuously until a time-independent plateau is observed. This asymptotic behavior is exhibited by all of the networks studied, irrespective of chain length, and is a consequence of the cross-linked network structure. The height of the displacement's long-time plateau, given in Table 4, depends on the network chain length and functionality, as well as on the presence of topological and steric constraints.

In order to pave the way for a discussion of our simulation results in light of existing network theories, we now briefly review the cross-link displacement predictions of the classical affine and phantom models. We also discuss the predictions of the constrained junction model of Flory and Erman[8,67] and the localization model of Vilgis and Boue[39,40] in some detail.

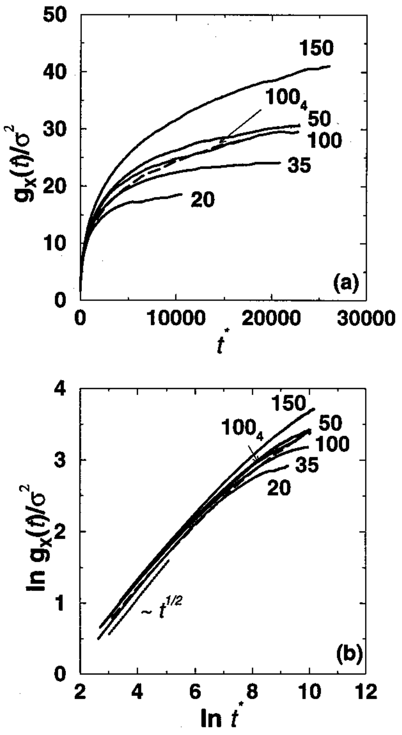

Figure 5. Mean-squared displacement of the cross-links, $g_x(t)/\sigma^2$, versus reduced time, t^*, for trifunctional networks of chain lengths 20, 35, 50, 100, and 150, and a tetrafunctional network of chain length 100 (dashed line): (a) a linear and (b) a log−log plot.

The phantom and affine models represent the extremes of junction behavior in networks. The affine model assumes that the junctions in an undeformed network remain stationary at their mean positions, i.e., that the cross-link displacement is zero, while the phantom model predicts that the junctions in an undeformed network fluctuate freely about their average positions with a mean-squared displacement (variance) given by $\langle(\Delta R)^2\rangle_{ph} = ((f-1)/f(f-2))\langle R^2(N)\rangle$, where $\langle R^2(N)\rangle$ is the mean-squared end-to-end distance of the unperturbed network chain (see Table 3). Since the junctions do undergo displacement, the affine model prediction is obviously incorrect. The phantom model predictions for the variance are shown in Table 4. From comparison with our simulation results for $g_x(t \rightarrow \infty)$, it is evident that the phantom model greatly overpredicts the junction displacement, except for the smallest chain lengths. The disparity between the phantom model prediction and the observed results can be attributed to excluded-volume and entanglement effects, neither of which is accounted for by the phantom model.

There are three main factors that affect the extent of junction displacement in real networks: the permanent attachment of the cross-links to the network structure, which restricts their free motion (the cross-link constraint), the presence of entanglement and steric effects, and the conditions under which the network was cross-linked. The effect of entanglement constraints on network junctions is addressed by the localization model of Vilgis and Boue,[39,40] and the constrained junction model of Flory and Erman.[8,67] Although these theories differ in their treatment of entanglements, both are based on the idea that the presence of topological constraints significantly damps the phantom-like fluctuations of the junctions.

In the localization model of Vilgis and Boue,[39,40] the asymptotic mean-squared displacement (MSD) of the cross-links in an f-functional network can be expressed in the following form,

$$[g_x(t\rightarrow\infty)]^{-1} = \frac{A}{\langle R_G^2(N)\rangle}\left(\frac{f}{2} - 1\right) + \frac{1}{\langle R_t^2\rangle} \qquad (14)$$

The first term represents the localization effect due to the cross-links in the absence of entanglement constraints and depends on the chain length (since $\langle R_G^2(N)\rangle \propto N$). The second term represents the enhanced localization effect due to entanglements or sliplinks; here $\langle R_t^2\rangle$ is the average radius of gyration of the chain between successive sliplinks and is of the order of the square of the tube diameter. The quantity A is a constant. If we just consider the localization of the junctions due to cross-linking (neglecting the second term), the asymptotic mean-squared displacement as predicted by eq 14 is directly proportional to the chain length and is inversely proportional to the network functionality. When the additional localizing effect on the junctions due to entanglements is considered, the asymptotic mean-squared displacement becomes a much weaker function of chain length, and as $N \rightarrow \infty$, $g_x(t\rightarrow\infty)$ becomes independent of chain length altogether (since the additional term $\langle R_t^2\rangle$ has been taken to be dependent on the chain entanglement length alone).[38]

In the constrained junction model of Flory and Erman,[8] the mean-squared displacement, $\langle(\delta r)^2\rangle$, of the cross-links from their mean positions is expressed in the following form,[8]

$$\frac{1}{\langle(\delta r)^2\rangle} = \frac{1}{\langle(\Delta R)^2\rangle_{\mathrm{ph}}} + \frac{1}{\langle(\Delta r)^2\rangle_{\mathrm{entangle}}} \qquad (15)$$

Paralleling eq 14, the first term on the right-hand side represents the cross-link constraint, and the second term represents the entanglement constraint. The strength of the cross-link constraint is taken to be the the inverse of the mean-squared fluctuation, $\langle(\Delta R)^2\rangle_{\mathrm{ph}}$, of the cross-link about the center of a phantom domain, and the strength of the entanglement constraint is taken to be the inverse of the mean squared fluctuation of the cross-link, $\langle(\Delta r)^2\rangle_{\mathrm{entangle}}$, about the center of a constraint domain. Hence, the stronger the entanglement constraint, the smaller the junction fluctuation will be.

A key idea of the constrained junction model is that the ratio of the strengths of the entanglement constraint and the cross-link constraint, κ, is proportional to the degree of interpenetration of the network, N_x^{av}, i.e.,

$$\kappa \equiv \frac{\langle(\Delta R)^2\rangle_{\mathrm{ph}}}{\langle(\Delta r)^2\rangle_{\mathrm{entangle}}} \propto N_x^{\mathrm{av}} \qquad (16)$$

From eq 9 and eq 16, the relative entanglement constraint strength, κ, is directly proportional to the square root of the chain length (since $\langle R^2(N)\rangle \propto N$). Substituting eq 16 into eq 15, the average displacement of a cross-link from its mean position can be rewritten as

$$\frac{1}{\langle(\delta r)^2\rangle} = \frac{1}{\langle(\Delta R)^2\rangle_{\mathrm{ph}}} + \frac{\kappa}{\langle(\Delta R)^2\rangle_{\mathrm{ph}}} \qquad (17)$$

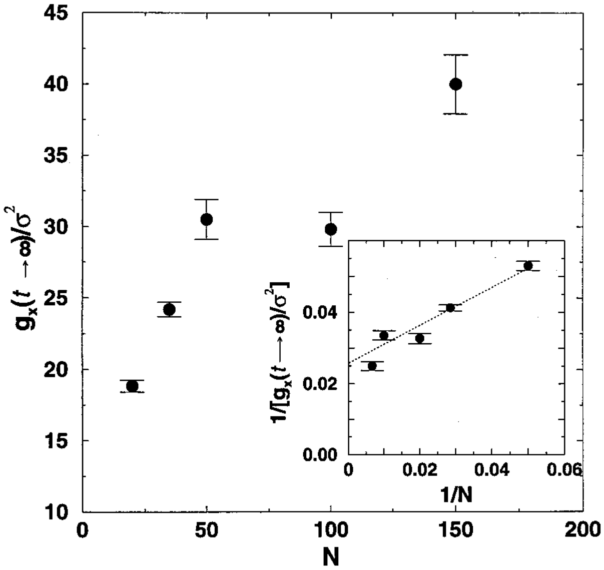

Figure 6. The asymptotic cross-link displacement, $g_x(t\rightarrow\infty)/\sigma^2$ for the trifunctional networks versus the chain length N. The inset shows the inverse asymptotic cross-link displacement versus $1/N$. The dotted line is a regression fit to the data (which excludes the 150-mer data point).

The average displacement of the cross-links about their mean positions under the influence of entanglements alone, represented by the inverse of the second term in eq 17, is proportional to the square root of the chain length (since $\kappa \propto N^{1/2}$ from eq 9 and eq 16, and $\langle(\Delta R)^2\rangle_{\mathrm{ph}} \propto N$). Although the above equation is expressed in terms of the variance, i.e., the average displacement of the cross-links from their mean positions, we expect the same scaling to be obeyed by the asymptotic mean-squared cross-link displacement, $g_x(t\rightarrow\infty)$.

A third factor that needs to be considered in an analysis of cross-link dynamics, is the influence of the cross-linking conditions on the final network properties. Since our networks were cross-linked at low packing fractions, the degree of interpenetration and hence of entanglement will be lower than in networks cross-linked at high packing fractions. Therefore we expect that the asymptotic MSDs will be larger for networks cross-linked at low packing fractions than for those cross-linked at high packing fractions. A small test simulation that confirms this reasoning is described under Dependence of Network Dynamics on Cross-Linking Conditions.

Our analysis of our cross-link MSD simulation results in terms of these three factors, i.e., the effects of cross-linking, entanglements, and cross-linking conditions, is presented below. The trends are compared with the predictions of the Vilgis and Boue localization model and the constrained junction model. We begin by ascertaining the scaling behavior of the cross-link MSD with chain length from Figure 6, in which the asymptotic MSD $g_x(t\rightarrow\infty)/\sigma^2$ is displayed versus N. At short chain lengths (20, 35, and 50), we find that $g_x(t\rightarrow\infty)$ is linearly dependent on the chain length, and we conclude that the cross-link constraint is dominant (cf. eq 14 and eq 17). At longer chain lengths, the displacement is much lower than would be expected if the cross-link constraint alone were operative and thus the asymptotic MSD scales differently with chain length. We see some anomalous results in the high-molecular-weight region of Figure 6; for instance, the cross-link displacement of the 100-mer is slightly lower than the displacement of the 50-mer. This is probably because the strength of the entanglement constraint is much greater in the 100-mer network than in the 50-mer network. Following the constrained junction model, we can obtain a measure of the relative entanglement constraint strength, κ, in the 100- and 50-mer networks from the ratio of the degrees of interpenetration of the networks. The ratio of the degrees of interpenetration of the 100- and 50-mer networks, $[N_x^{av}]_{100}/[N_x^{av}]_{50} \approx 2$ (from Table 4), whereas the predicted ratio from eq 9 is only $\sim(100/50)^{1/2} = 1.414$, confirming the presence of a stronger entanglement constraint in the 100-mer network than in the 50-mer network. In addition, the fact that the cross-link displacements for the 50- and 100-mer networks are quite similar in magnitude suggests that, for the 100-mer chains, the effect of cross-linking is weak compared to the effect of entanglements.

The displacment for the 150-mer network is considerably larger than those for the 50- and 100-mer networks, probably because of the difference in initial cross-linking densities. The 150-mer network was cross-linked at a packing fraction ($\phi_{ini} = 0.15$), which is lower than that at which the 50- and 100-mer networks were cross-linked ($\phi_{ini} = 0.26$), which means that its chains are considerably less interpenetrated than if it had been cross-linked at a packing fraction of 0.26. Hence, the MSD observed for the 150-mer network is much larger than those observed for the 50- and 100-mer networks.

We now attempt to check whether our results support the localization model of Vilgis and Boue or the constrained junction model, even though the relative paucity of data in the high-molecular-weight region makes it difficult to reach a definitive conclusion. Since our data for the longer chain lengths in Figure 6 appear to be relatively independent of chain length (neglecting the 150-mer data point since its MSD is large due to its initial cross-linking at a low packing fraction), we think that our results are more in keeping with the tube model picture of Vilgis and Boue than with the constrained junction model. We can then use the Vilgis and Boue model to obtain an approximate idea of the network tube diameter R_t from the inset of Figure 6, which shows a plot of $1/g_x(t\rightarrow\infty)$ versus $1/N$. A linear regression fit of the data (excluding the 150-mer point) in the inset (dotted line) yields an intercept of $\sim$0.025 in the limit of infinite molecular weight, so that a squared network tube diameter of $R_t^2 \sim 40\sigma^2$ is obtained (from eq 14). We can obtain the network entanglement length $N_e^{network}$ by setting $R_t^2 = 2\langle R^2{}_G(N_e^{network})\rangle$ (following a similar analysis for melts.[41,62] $N_e^{network}$ turns out to be $\sim$70. These values of R_t^2 and entanglement length are much larger than the corresponding values obtained by Smith et al. in their hard-chain melt studies;[62] they obtained $2\langle R_G^2(N_e)\rangle \approx 20.9\sigma^2$ and $N_e \approx 35$ at $\phi = 0.4$, and $2\langle R_G^2(N_e)\rangle \approx 15.8\sigma^2$ and $N_e \approx 29$ at $\phi = 0.45$. Assuming that the network tube diameter from eq 19 is indeed comparable to the melt tube diameter obtained from a tube model-based analysis of melt simulation data,[62] the difference between the melt tube diameter and the extrapolated network tube diameter can be attributed to the cross-linking of our networks at low densities. Even though the network density after cross-linking was raised to the melt density, the influence of the cross-linking conditions remains “frozen” in the system and results in the networks chains being less entangled than they are in the melt. This would account for the network tube diameters and entanglement lengths in our studies being larger than those from the melt simulations. The networks from the Duering et al. studies have tube diameters and entanglement lengths similar to their melt studies since their cross-linking was done at meltlike densities. To see whether our network tube diameters bear any relation to the un-cross-linked-chain tube diameters at the initial cross-linking densities, we use the melt tube diameters from the Smith et al.[62] study to estimate the tube diameters for un-cross-linked chains at packing fractions of $\phi = 0.26$ and $\phi = 0.3$. The initial cross-linking densities are taken from Table 2. The tube diameters are estimated using the relation,[53,71] $R_t(\phi) = R_t(\phi_{melt})(\phi/\phi_{melt})^{-0.75}$, where ϕ_{melt} and $R_t(\phi_{melt})$ are the packing fraction and tube diameters at melt densities, which are taken from the work of Smith et al. The square of the tube diameter for un-cross-linked chains is $\sim 36\sigma^2$ at $\phi = 0.26$, and $\sim 30\sigma^2$ at $\phi = 0.3$, which is fairly close to the network tube diameter value obtained above.

The dependence of the cross-link displacement on the initial cross-linking conditions is also manifested in the difference between our MSD results and those of Duering et al. for 100-mer networks. The magnitude of the cross-link MSD of our 100-mer tetrafunctional network is much larger than that of the corresponding 100-mer tetrafunctional network of Duering et al.:[38] since our tetrafunctional network was cross-linked at an initial packing fraction of 0.15, its degree of interpenetration and extent of entanglements is likely to be much lower and the cross-link MSD correspondingly larger than the network of Duering et al. Our trifunctional 100-mer network cross-link displacements are also larger than those of the tetrafunctional 100-mer from the studies of Duering et al. This is due to the difference in functionality as well as to the difference in the cross-linking method.

(2) Mean-Squared Displacement of the Inner Segments of the Chains. Panels a and b of Figure 7 show the reduced mean-squared displacement of the inner segments of the network chains, $g(t)/\sigma^2$, versus reduced time, t^*, on linear and natural log scales, respectively. A study of the motion of the inner chain segments is of interest since their mobility is much greater than that of the cross-linked chain ends. In fact, their motion is considered to typify the behavior of much longer chains than can be studied by computer simulations. The MSD for the k inner segments of a chain is calculated as

$$g(t) = \frac{1}{k}\sum_{i=N/2-k/2}^{N/2+k/2}\langle|r_i(t+t_0) - r_i(t_0)|^2\rangle \qquad (18)$$

where the averaging is over all the chains and time origins, t_0. The value of k is chosen to be 2 for the 20-mer network, 4 for the 35- and 50-mer networks, 8 for the 100-mer networks, and 10 for the 150-mer network.

The inner segment MSD initially increases with a $t^{1/2}$ scaling, in agreement with the Rouse model predictions. As time increases, the slope of the MSD decreases continuously and shows a clear plateauing behavior at long times. This is very different from the inner segment displacement of long melt chains, in which the initial $t^{1/2}$ scaling is followed by a continuous increase in the mean-squared displacement with time.[41,62] The plateau values of the network inner segment MSD are reported in Table 4. These values are of interest since

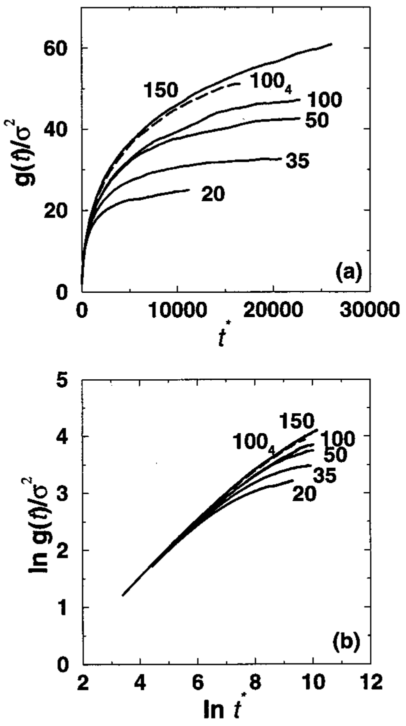

Figure 7. Mean-squared displacement, $g(t)/\sigma^2$, of the inner monomers of the network chains versus reduced time, t^*, for all chain lengths: (a) a linear and (b) a log–log plot. The dashed lines represent the 100-mer tetrafunctional network.

they reflect the cross-link and entanglement constraints on the network chains.

In order to interpret our inner segment MSD results from the standpoint of theoretical work in this area, we now briefly review the work of Vilgis and co-workers,[39,69,72] and of Duering et al.[38] The mean field theory of Vilgis and co-workers[39,69,72] predicts that the displacement of an inner segment k on a network chain obeys the relation,

$$g_k(t) \approx \left[\frac{(3k_BT/\zeta l^2)t}{1 + q_0^2(3k_BT/\zeta l^2)t}\right]^{1/2} \tag{19}$$

where ζ is the friction factor and λ is the segment diameter. At short times, the above equation predicts that the segment displacement follows the Rouse model scaling of $t^{1/2}$. At long times, the equation predicts the plateauing of the segmental motion, signifying that the chain is confined to a region of size q_0^{-1} where q_0^{-1} is of the order of the chain's mean-squared radius of gyration. Since entanglements are not taken into account, the theory predicts a scaling of $g(t\to\infty) \propto N$ (since $q_0^{-1} \propto \langle R_G^2\rangle \propto N$ at meltlike densities).

Duering et al. adopted a phenomenological approach[38] based on the tube model to account for entanglement constraints on segmental motion. Since the network chains cannot diffuse along the tube due to network connectivity, the inner segment displacement is not expected to display the second $t^{1/2}$ scaling region or the final t^1 tube disengagement region. Duering et al. hypothesized that the maximum value of the mean-squared displacement would be of the order of the melt chain displacement at the end of the $t^{1/4}$ scaling region, when the chain has internally relaxed within the tube ($g(t) \propto N^{1/2}$). Based on this hypothesis, they obtain the relation

$$g^{-1}(t\to\infty) = \frac{1}{2\langle R_G^2(N_e)\rangle}\left(\frac{N_e}{N}\right)^{1/2} \tag{20}$$

which is in keeping with their cross-link displacement observations. From their plot of $g^{-1}(t\to\infty)$ versus $N^{-1/2}$ (Figure 11c of ref 38) it appears that although their segment displacements scale approximately with $N^{1/2}$, their simulation data are somewhat overestimated by the slope of $N_e^{1/2}/2\langle R_G^2(N_e)\rangle$.

In order to facilitate a comparison of our simulation results to the above theoretical predictions, we present a graph of the asymptotic inner segment displacement $g(t\to\infty)/\sigma^2$ versus N, in Figure 8. From the figure, it is apparent that the asymptotic inner segment displacement scales linearly with the chain length at low molecular weights, in accordance with the prediction of Vilgis and co-workers (eq 19). At longer chain lengths, the displacements appear to have a weaker dependence on chain length. This is similar to our observations for the asymptotic cross-link displacements and suggests, based on the constrained junction and Vilgis and Boue models, that the asymptotic inner segment displacement for the longer chain lengths is lower than it would have been if the chains had been subject to cross-link constraints alone, due to the presence of additional entanglement-type constraints. To compare our results with the tube model-based prediction of Duering et al., we plot $g(t\to\infty)/\sigma^2$ versus $N^{1/2}$ in the inset of Figure 8. Since it does not appear that our inner segment MSD scales linearly with $N^{1/2}$ at long chain lengths, we conclude that our simulations do not show good agreement with the tube-type model of Duering et al.

Our inner segment MSDs are much larger than those seen by Duering et al., in keeping with our observation for the cross-link displacement. The disparity in the MSDs is partly due to the difference in network functionality, but an additional significant contribution comes from the differences in network topology due to the cross-linking techniques (as discussed previously in the section on cross-link displacements).

(3) Dependence of Network Dynamics on Cross-Linking Conditions. In this section, we describe a study specifically directed toward establishing the extent to which cross-linking conditions affect the dynamics of networks. To this end, we constructed and analyzed two small trifunctional networks consisting of 90 100-mers, which were initially cross-linked from the melt at packing fractions of 0.15 and 0.43. The packing fraction of the first system was then increased to a value of 0.43. Both networks were then allowed to relax for 2 billion collisions, and the generated trajectories were analyzed.

The structural characteristics of these networks are presented in Table 5. The networks have similar numbers of saturated junctions, unsaturated junctions, and dangling ends, which means that both systems have approximately the same elastically active fraction. The mean-squared end-to-end distance of the network chains is much lower for the $\phi_{\rm ini} = 0.15$ network (i.e., the network cross-linked at 0.15 and relaxed at 0.43) than for the $\phi_{\rm ini} = 0.43$ network (the network cross-linked and relaxed at 0.43), confirming our previous hypothesis that the chains are significantly contracted in networks cross-linked at low densities. The mean-squared displacements of the inner chain segments (solid lines) and cross-links (dashed lines) versus reduced time for both

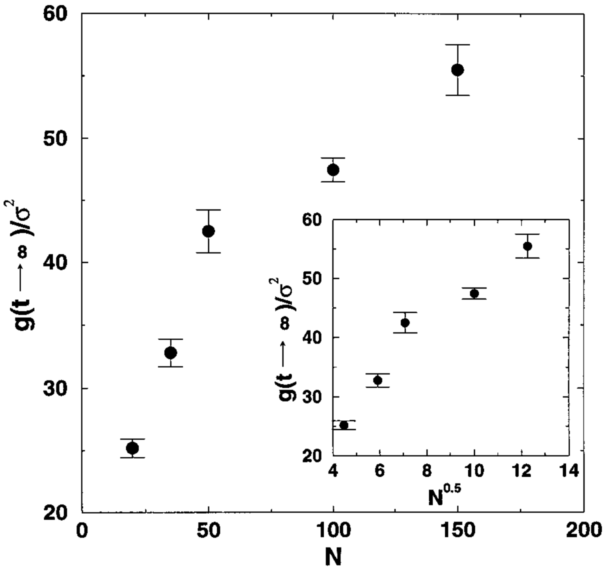

Figure 8. The asymptotic inner segment displacement, $g(t\rightarrow\infty)/\sigma^2$, for the trifunctional network versus the chain length, N. Inset shows the asymptotic displacement versus $N^{0.5}$.

Table 5. Simulation Results for Test Systems of Two Trifunctional 100-Mer Networks Cross-Linked at Different Initial Packing Fractions, ϕ_{ini}[a]

N	ϕ_{ini}	N_{sat}	N_2	N_{end}	x_{elastic}	$\langle R^2\rangle/\sigma^2$	N_x^{av}	$g_x(t\rightarrow\infty)/\sigma^2$	$g(t\rightarrow\infty)/\sigma^2$
100	0.15	53	7	7	0.88	123.83	6.13	31.3	44.7
100	0.43	53	7	7	0.77	161.55	6.83	25.01	41.9

[a] Both the networks are analyzed at $\phi = 0.43$. The structure and properties of the networks is given in terms of the number of saturated junctions, N_{sat}, number of unsaturated (bifunctional) junctions, N_2, number of dangling ends, N_{end}, the elastically active fraction, x_{elastic}, the chain mean-squared end-to-end distance $\langle R^2\rangle/\sigma^2$, the degree of interpenetration, N_x^{av}, and the long-time MSDs of the cross-links and chain inner segments, $g_x(t\rightarrow\infty)/\sigma^2$ and $g(t\rightarrow\infty)/\sigma^2$.

networks are shown in Figure 9, and the asymptotic values of the long-time displacements are reported in Table 5.

From Figure 9, we observe that the MSDs for the $\phi_{\text{ini}} = 0.15$ network considerably exceed those of the $\phi_{\text{ini}} = 0.43$ network. If we consider the asymptotic cross-link MSD, the value of $g_x(t\rightarrow\infty)$ for the $\phi_{\text{ini}} = 0.15$ network is 31.3, while the value of $g_x(t\rightarrow\infty)$ for the $\phi_{\text{ini}} = 0.43$ network is 25.01 (see Table 5). The disparity in the MSDs can be related to the fact that the degree of interpenetration (see section on Static Structure Factor of the Cross-Links) of the, $\phi_{\text{ini}} = 0.15$ network ($N_x^{\text{av}} = 6.13$) is lower than that of the, $\phi_{\text{ini}} = 0.32$ network ($N_x^{\text{av}} = 6.83$), which is in turn related to the lower end-to-end distance of the $\phi_{\text{ini}} = 0.15$ network chains ($\langle R^2\rangle = 123.83$) relative to the $\phi_{\text{ini}} = 0.43$ network ($\langle R^2\rangle = 161.55$). Since the 0.15 network chain sweeps out a smaller volume around it than the 0.43 network chain, it has a lower average number of cross-links per chain volume and hence a larger MSD.

An additional reason for the disparity in MSDs may be the difference in the proportion of trapped entanglements. It has been suggested in the literature[5,50,71] that networks that are formed in solution (i.e., at low density) contain a lower proportion of trapped entanglements compared with networks that are cross-linked in the bulk (i.e., at high density). Although it is difficult to quantify the number of trapped entanglements, we would expect that since the melt chains are themselves less entangled at the lower density, the 0.15 network would have a lower trapped entanglement contribution than the 0.43 network, because the process of cross-linking "freezes in" the melt chain configurations. Hence, the 0.15 network will have a higher MSD than the 0.43 network.

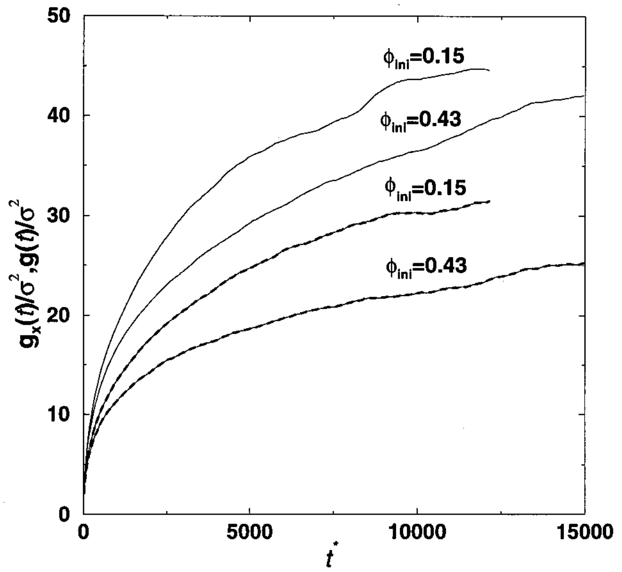

Figure 9. Reduced inner segment displacements, $g(t\rightarrow\infty)/\sigma^2$, (solid lines) and cross-link displacements, $g_x(t\rightarrow\infty)\sigma^2$, (dashed lines) versus reduced time, t^*, at a packing fraction of 0.43 for two 100-mer trifunctional test networks initially cross-linked at packing fractions of $\phi_{\text{ini}} = 0.15$ and $\phi_{\text{ini}} = 0.43$.

Although the size of the samples in the above study is not large enough to exclude finite size effects, the trends are sufficient to confirm that the conditions at cross-linking have a major impact on the properties of networks and should be given consideration in studies of network dynamics.

(4) Intermediate Scattering Function. Additional information on the network dynamics can be obtained by calculating the intermediate scattering function for the chains and cross-links. The intermediate scattering function is a measure of local density variations in the system, and is particularly useful in probing network dynamics since it can be measured directly from neutron scattering and spin echo experiments.[73]

We can measure either the intermediate *incoherent* scattering function, which describes the motion of a single segment in the system, or the *coherent* scattering function, which describes the motion of pairs of scattering segments. The intermediate incoherent scattering function $S_{\text{inc}}(\mathbf{q}, t)$ is related to the self-correlation function and is defined as

$$S_{\text{inc}}(\mathbf{q}, t) \equiv \frac{1}{N}\sum_{i=1}^{N}\langle\exp(i\mathbf{q}\cdot[\mathbf{r}_i(t+t_0) - \mathbf{r}_i(t_0)])\rangle \quad (21)$$

The averaging is done over all N segments in the fluid and over all time origins t_0. The intermediate coherent scattering function $S(\mathbf{q}, t)$ measures density correlations along a single chain, and is given by

$$S(\mathbf{q}, t) = \frac{1}{N}\sum_{j=1}^{N}\sum_{i=1}^{N}\langle\exp(i\mathbf{q}\cdot[\mathbf{r}_i(t+t_0) - \mathbf{r}_j(t_0)])\rangle \quad (22)$$

where *i* and *j* are segments along the same chain. The averaging is done over all *N* chains in the network, over all time origins t_0, and over orthogonal scattering vectors having identical magnitudes.

We now briefly review some of the theoretical predictions for the intermediate coherent scattering function of melt chains, since we will use them to interpret our simulation data for networks. The coherent scattering function of a single melt chain can be calculated analytically within the Rouse[70] and reptation models.[74] For the Rouse model, rigorous calculations have been performed[70] which yield simplified expressions for specific wave vector and time domains. In the limit of small wave vectors and long times, i.e., $\mathbf{q}^2\langle R_G^2\rangle \ll 1$, $t < \tau_R$, a regime that describes the overall diffusion of the chain, the scattering function decays exponentially with time as,

$$S(\mathbf{q},\, t)/S(\mathbf{q},\, 0) = \exp(-D(\mathbf{q}\sigma)^2 t) \tag{23}$$

where *D* is the self-diffusion constant of the center of mass of the chain (given by $D \equiv k_B T/N\zeta$). In the limit of large wave vectors, i.e., $\mathbf{q}^2\langle R_G^2\rangle \gg 1$, the internal relaxation of the chain is described, and the scattering function simplifies to

$$S(\mathbf{q},\, t)/S(\mathbf{q},\, 0) = \exp\left(-\frac{2}{\sqrt{\pi}}(\Gamma_q t)^{1/2}\right) \tag{24}$$

where the quantity Γ_q is wavevector dependent and is given by[70] $\Gamma_q = k_B T(\mathbf{q}\sigma)^4\langle R^2\rangle/12\zeta N$. According to the Rouse model, if the logarithm of the normalized scattering function $S(\mathbf{q}\sigma,t)/S(\mathbf{q}\sigma,0)$ is plotted against $(\mathbf{q}\sigma)^2 t^{1/2}$, one curve should be obtained for all values of $\mathbf{q}\sigma$. In addition, the scattering function should be independent of chain length since the internal motion does not depend on the size of the chain.

The reptation model[74] suggests that the restriction of chains in a melt to specific spatial domains due to entanglement constraints will cause the coherent scattering function to plateau at long times. In the time regime $\tau_E < t < \tau_R$, when the melt chain undergoes local diffusion along the tube, the coherent scattering function for the wave vector range $1/D_t > \mathbf{q}\sigma/2\pi > 1/(\langle R^2(N)\rangle)^{1/2}$ is given by

$$S(\mathbf{q},\, t)/S(\mathbf{q},\, 0) = 1 - (\mathbf{q}D_t)^2/36 \tag{25}$$

where D_t^2 is defined as the square of the end-to-end distance of a chain of entanglement length N_e and is of the order of the square of the tube diameter. The value of D_t^2 is expected to be independent of chain length and wave vector.

We now compare and contrast our simulation results for the network chain intermediate coherent scattering function with the melt theoretical predictions described above. Figure 10 displays a semilogarithmic plot of the normalized coherent scattering function versus Rouse scaled time $(\mathbf{q}\sigma)^2 t^{*1/2}$ for the 35-, 50-, and 100-mer trifunctional networks. The wave vectors for each network are chosen such that the internal relaxation of the chain is probed, i.e., $\mathbf{q}\sigma \gg 1/(\langle R^2(N)\rangle^{1/2})$. At short times, for all the chain lengths, the curves collapse onto each other in the region $(\mathbf{q}\sigma)^2 t^{*1/2} < 10$, satisfying the Rouse model prediction from eq 24.

At longer times, the scattering function curves decay to a wave vector-dependent plateau. The existence of a plateau for all chain lengths including the 35-mer network suggests that plateau formation is associated with the spatial localization of the network chains due to the cross-linked structure as well as with entanglement and steric effects (analogous to the asymptotic cross-link and inner segment displacement plateaus). We can apply eq 25 (the reptation equation) to our long-time scattering function results to obtain network tube diameters that can be compared with those from our cross-link displacement calculations (see section on Mean-Squared Displacement of the Cross-Links). For instance, if we choose a curve such that the corresponding wave vector satisifies the relation $\mathbf{q}\sigma/2\pi > 1/(\langle R^2(N)\rangle^{1/2})$, e.g., the curve $\mathbf{q}\sigma = 0.96$ for 50-mers in Figure 10b, we can use eq 25 to obtain the square of the tube diameter D_t^2 to be $\sim 38\sigma^2$, which agrees fairly well with the value of $R_t^2 \sim 40\sigma^2$ that we obtained from the cross-link mean-squared displacement calculations in the section on Mean-Squared Displacement of the Cross-Links. For scattering curves corresponding to a particular wave vector, the tube diameters obtained using eq 25 are approximately the same for the 35-, 50-, and 100-mer networks, which is in accordance with tube model theory. In contradiction to the tube model theory, however, our tube diameters are not independent of the wave vector; for instance, the scattering curve corresponding to the wave vector $\mathbf{q}\sigma = 0.78\sigma$ yields a squared tube diameter, $D_t^2 \sim 54\sigma^2$, while the scattering curve corresponding to the wave vector $\mathbf{q}\sigma = 1.18$ yields a squared tube diameter, $D_t^2 \sim 26\sigma^2$. This inconsistency between theory and simulation results may be because eq 25 was not applied strictly within the appropriate wave vector range (i.e., $\mathbf{q}\sigma/2\pi$ may not be smaller than

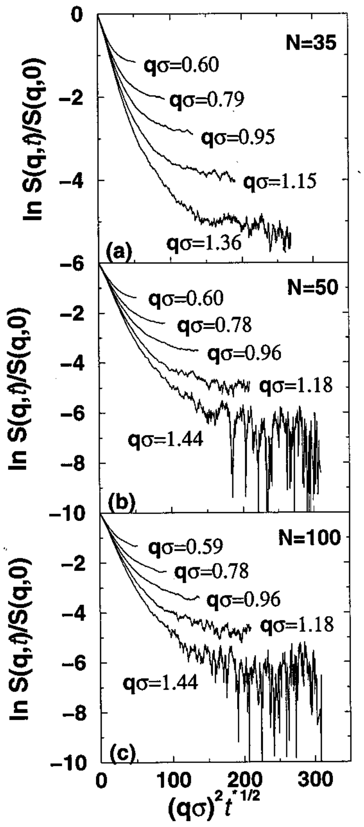

Figure 10. Normalized intermediate scattering function, $S(\mathbf{q}, t)/S(\mathbf{q}, 0)$, versus Rouse scaled time, $(\mathbf{q}\sigma)^2 t^{*1/2}$: (a) 35-, (b) 50-, and (c) 100-mer trifunctional networks. Each curve is labeled with the magnitude of the corresponding wave vector, $\mathbf{q}\sigma$.

$1/D_t$). Another source of error may be that eq 25 cannot be applied directly to network chains without accounting for the cross-link constraint.

Our observations regarding the intermediate scattering function are qualitatively consistent with the findings of Duering et al. in their tetrafunctional network study. They too observed an initial Rouse-like decay of the scattering function followed by plateau at long times. While they found that the tube diameters obtained by using the reptation equation agreed with their cross-link displacement results, their tube diameters were not independent of the chain length. They did not comment on the wave vector dependence of the scattering function.

Elastic Modulus. The elasticity of rubberlike networks has been the subject of numerous experimental studies aimed at probing the relation between the elastic moduli and the molecular structure. Experimental elastic moduli are typically measured in the small strain regime by conducting simple extension or stress relaxation experiments to determine the tensile or shear relaxation moduli, respectively; however, deductions about structure−property relations are hampered by the difficulty associated with characterizing the network molecular structure in sufficient detail. Computer simulations provide an excellent tool to investigate structure−moduli relationships, provided that the elastic moduli can be computed in a straightforward manner. In a simulation, the use of methods similar to experimental techniques to calculate the moduli would necessitate deforming the sample and then allowing it to relax for extremely long time periods, a procedure that is computationally very expensive given the size of the network systems and the fact that we have already allowed the networks to relax for long times. We therefore adopt a method suggested by Duering et al.,[38] based on the original development of Doi and Edwards,[70] to calculate the network relaxation modulus using the existing trajectories from our simulations.

According to Doi and Edwards, the shear relaxation modulus for Gaussian chains in an un-cross-linked melt is given within the Rouse and reptation models, by

$$G(t) = \frac{N_c k_B T}{V} \sum_{p=1}^{\infty} \exp(-2tp^2/\tau_R) \qquad (26)$$

The above equation can be expressed in terms of the normal or Rouse modes of the chains (measures of the internal chain structure). The Rouse modes of a chain with discrete segmental positions are given by[70]

$$X_p(t) = \frac{1}{N} \sum_{i=1}^{N} \left[r_i(t) \cos\left(\frac{p\pi i - 1}{N - 1}\right)\right] - \frac{1}{2N} [r_1(t) + (-1)^p r_N(t)] \qquad (27)$$

where each mode represents the local motion of a chain with N/p segments. The shear relaxation modulus can be written in terms of the autocorrelation of the Rouse modes[38,41] as

$$G(t) = \frac{c}{N} k_B T \sum_p \frac{\langle X_p(2t) X_p(0)\rangle}{\langle X_p^2\rangle} \qquad (28)$$

where $\langle X_p^2\rangle = \langle X_p(0)X_p(0)\rangle$ is the amplitude of the pth mode. The plateau modulus is given by the long time limit of the time-dependent shear relaxation modulus, i.e.,

$$G_e \sim \lim_{t\to\infty} G(t) \qquad (29)$$

Since the above analysis applies to Gaussian chains with un-cross-linked ends, Duering et al. constructed several random walk paths along the network such that the walks began and ended at segments that were not cross-linked. The Rouse modes of these walks were then used to calculate the network relaxation modulus. The moduli calculated using the above approach may not coincide exactly with the moduli calculated from a stretching or shear experiment. Nevertheless, they are expected to display the same trends with time and chain molecular weight as the latter. Hence, the moduli calculated from the Rouse modes of the network chains will provide excellent qualitative insights into the elastic behavior of networks.

The above procedure was adopted by us to calculate the network moduli. We constructed random walks along the network such that the path lengths were larger than the original network chain lengths (for the most part, paths of length $2N$ were employed, but we found, following Duering et al., that the path length did not affect the results) e.g., paths of length 40 for the 20-mer system, 70 for the 35-mer system, 100 for the 50-mer networks, and 200 for the 100-mer networks. In most cases, 32 such walks were constructed. The paths were chosen such that the loops and dangling ends were avoided. The Rouse modes of these walks were calculated and used in accordance with eq 28 to obtain the time-dependent modulus. Prior to doing this, we checked that the constructed paths were Gaussian.

In an effort to confirm that the constructed walks were Gaussian, we calculated the amplitude of their Rouse modes, $\langle X_p^2\rangle$. For a Gaussian chain, the Rouse mode amplitude obeys the scaling relation

$$\langle X_p^2\rangle = \frac{\langle R^2\rangle}{2\pi p^2} \qquad (30)$$

Figure 11 shows $2\pi\langle X_p^2\rangle$ plotted against p^2 on a logarithmic scale for the 20-, 35-, 50-, and 100-mer networks. Since the slope of the plot ~ -1 as expected, we conclude that the constructed random walks are Gaussian and could be used in conjunction with eq 28 in the calculation of the network modulus.

The reduced network moduli calculated from eq 28 are presented in Figure 12 as a function of time for each of the trifunctional systems and for the 100-mer tetrafunctional network. All the moduli show an initial decrease followed by a time-independent plateau at long times. The asymptotic values of the reduced modulus, $G_e\sigma^3$, from Figure 12 are reported in Table 6.

In order to assess the effect of cross-linking, it is useful to compare the time-dependent behavior of network and melt moduli. As shown in Figure 12, the modulus for a network initially decreases with time and then reaches a plateau value which does not change further even at very long times.[65] In contrast, the modulus for a long-chain polymeric melt reaches a chain length-independent plateau at intermediate times, which is attributed to entanglement effects, before again decreasing with time. (The reptation model[70] predicts that this plateau will occur on a time scale $\tau_e < t < \tau_d$,

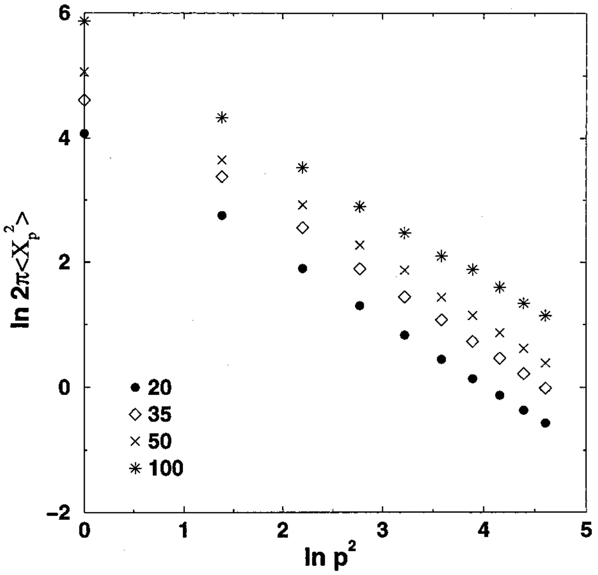

Figure 11. Amplitude of the Rouse modes, $2\pi^2\langle X_p^2\rangle$, versus the square of the mode number, p^2, on a log−log plot for trifunctional networks of chain length 20, 35, 50, and 100.

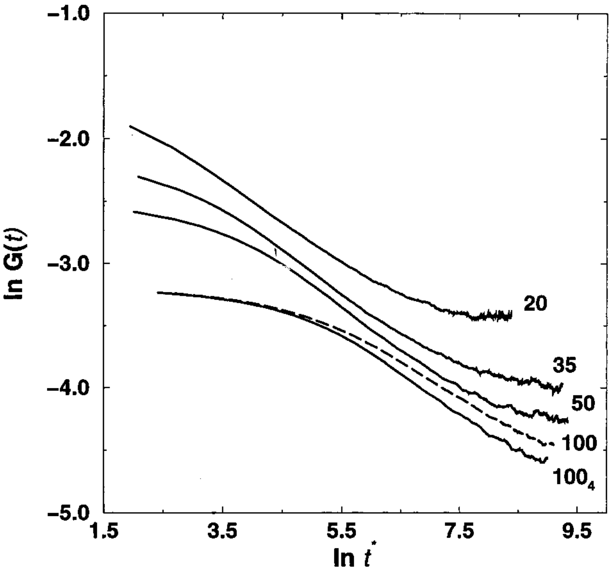

Figure 12. Time-dependent reduced moduli, $G(t)\sigma^3$, versus reduced time, t^*, on a log−log plot for four trifunctional networks and the 100-mer tetrafunctional network (dashed line).

Table 6. Elastic Moduli from Simulation, $G_e\sigma^3$, Compared to the Predictions of the Affine Model, $G_e^{\text{affine}}\sigma^3$, and the Phantom Model, $G_e^{\text{phantom}}\sigma^3$ [a]

N	$G_e\sigma^3$	$G_e^{\text{affine}}\sigma^3$	$G_e^{\text{phantom}}\sigma^3$	$\langle R^2\rangle/\langle R_0^2\rangle$
20	0.039(0)	0.037	0.012	0.943
35	0.023(1)	0.021	0.008	0.952
50	0.018(1)	0.015	0.005	0.939
100	0.015(1)	0.0067	0.0025	0.927
100_{tetra}	0.011(1)	0.0078	0.00265	0.835

[a] The ratio of the mean-squared end-to-end distances of a network chain and a melt chain at the same packing fraction is given by $\langle R^2\rangle/\langle R_0^2\rangle$. Values in parentheses give the error in the last digit of $G_e\sigma^3$.

when the chain is reptating along the tube. Beyond τ_d, the modulus of the melt is supposed to decrease with time as the chain disengages from the tube.)

The network plateau modulus corresponds to the equilibrium elastic modulus predicted by the theories of rubber elasticity. The classical affine model predicts the following form for the elastic modulus of a perfect network

$$G_e^{\text{affine}} = \frac{\langle R^2\rangle}{\langle R_0^2\rangle}\nu k_B T \qquad (31)$$

where $\nu = N_a/V \approx 6\phi/\pi N$ is the number of elastically active network chains per unit volume and the fraction $\langle R^2\rangle/\langle R_0^2\rangle$, the so-called memory factor,[75] is the ratio of the end-to-end distance of an undeformed network chain to the end-to-end distance of a melt chain at the same density. This ratio is usually set to 1 if the network is formed from a melt at the same density. Since our networks have been formed from a system of linear chains at a lower initial density, the values of $\langle R^2\rangle/\langle R_0^2\rangle$ for our systems are considerably less than 1 and must be explicitly incorporated into eq 31. Table 6 shows the values of $\langle R^2\rangle/\langle R_0^2\rangle$ which are calculated using $\langle R^2\rangle$ from our simulations (see Table 3) and $\langle R_0^2\rangle$ from the melt simulation data of Smith et al.[62] The phantom model prediction for the elastic modulus, G_e^{phantom}, takes a form similar to eq 31 except that the number of active chains per unit volume ν in eq 31 is replaced by the term $\nu - \mu$, where μ is the number of elastically active junctions. Since the affine and phantom model treatments supposedly represent the two extremes of junction behavior in networks, the elastic moduli of real networks would be expected to lie between the affine and phantom moduli predictions, with the affine modulus representing an upper limit and the phantom modulus a lower limit. The predictions of the affine and phantom model for our networks are presented in Table 6. The values of N_a and μ for these calculations are obtained from Table 1.

A comparison of the simulation moduli with the phantom prediction shows that the moduli from all of our stimulations are much larger than the latter, as expected. Interestingly our network moduli also exceed the affine model predictions, although the moduli for the networks of shorter chain length, 20, 35, and 50, are only slightly larger than the affine model predictions. This is probably due to the affine model's neglect of excluded-volume interactions. The modulus for the longer chain 100-mer network is considerably larger than the affine model value. Similar observations were made by Duering et al. even though the structure of their network is somewhat different from ours with respect to the contribution from chain interpenetration and entanglements.

The fact that the observed moduli exceed the affine model prediction has been ascribed by Langley[42] and Graessley and co-workers[64,76] to an additional contribution to the modulus from entanglement constraints in long-chain networks. Graessley and co-workers proposed that the modulus takes the form

$$\begin{aligned} G_e &= G_e^{\text{affine/phantom}} + G_e^0 T_e \\ &= \frac{\langle R^2\rangle}{\langle R_0^2\rangle}(\nu - h\mu)k_B T + G_e^0 T_e \qquad (32) \end{aligned}$$

where the empirical parameter h ($0 < h < 1$) is used to account for the partial suppression of junction fluctua-

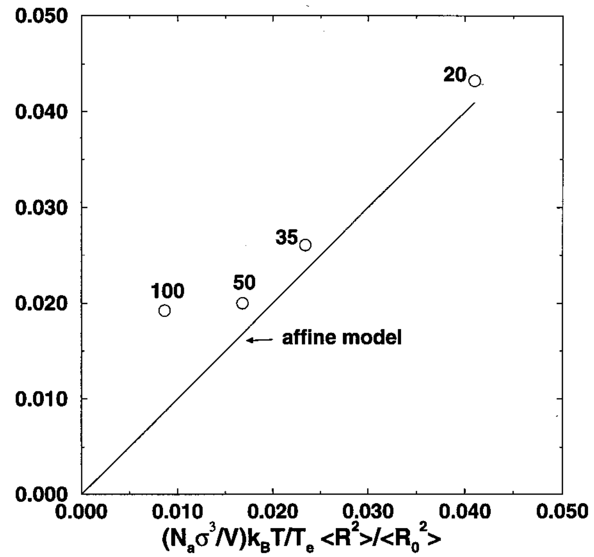

Figure 13. Plateau values of the reduced modulus, $G(t \to \infty)\sigma^3$, scaled by the trapping factor, T_e, versus the number of elastically effective chains per unit volume, $\nu = N_a\sigma^3/V$, scaled by T_e and the memory factor, $\langle R^2\rangle/\langle R_0^2\rangle$. The solid line represents the affine model prediction.

tions by entanglements in real networks between the affine ($h = 0$) and phantom ($h = 1$) limits, G_e^0 is a maximum possible modulus, and T_e is a factor that incorporates the contribution of trapped entanglements. T_e is considered to be equal to the probability that all four paths leading away from a randomly chosen pair of un-cross-linked segments lead independently to the network.[64,76] When $h = 0$, the junction fluctuations are completely suppressed (as in the affine model), and G_e^0 is set to G_N^0, the plateau modulus of the equivalent melt; thus, the modulus of a real, highly entangled network is equal to the sum of the classical affine contribution plus an additional entanglement contribution that is proportional to the modulus of the equivalent entangled melt.

The magnitude of the trapped entanglement contribution to the moduli of our networks can be ascertained by comparing the asymptotic values of $G(t)$, G_e, with the predictions of the affine model. We present a Langley plot of the scaled asymptotic modulus $G_e\sigma^3/T_e$ for the trifunctional networks versus $(N_a\sigma^3/V)k_BT/T_e(\langle R^2\rangle/\langle R_0^2\rangle)$ in Figure 13 (since $\nu = N_a/V$). For near-perfect networks, $N_a/V \approx 6\phi/\pi N$, so that, at constant packing fraction, Figure 13 displays the scaled asymptotic moduli versus inverse chain length. Following Graessley and co-workers,[64,76] we have calculated T_e as the square of the elastic fraction, i.e., $T_e \approx (x_{\mathrm{elastic}})^2$ (the values of x_{elastic} are taken from Table 1). The solid line in Figure 13 shows the affine modulus calculated from eq 31. Our moduli exceed the affine prediction for all the networks studied, and we attribute this to a combination of excluded-volume and trapped entanglement effects (based on the Langley−Graessley model). The data in Figure 13 show two different scales—a higher slope for chain lengths 20, 35, and 50 that parallels the affine prediction and a lower slope beyond the 50-mer, indicating that trapped entanglements play a more important role in high-molecular-weight networks.

We now compare our simulation observations to experimental results in the literature. The form of the data in Figure 13 agrees very well with the results of the shear relaxation experiments on end-linked PDMS networks reported by Rennar and Opperman[26] and Patel et al.[27] Both groups observed that, for networks at low chain length (large N_a/V), the modulus decreased proportionally with molecular weight, and for networks with moderate to high chain lengths (intermediate N_a/V), the modulus remained fairly constant with molecular weight. This corroborates our observations from Figure 13, since N_a/V is inversely proportional to the chain length (molecular weight) for systems at constant packing fraction. In addition, Rennar and Opperman also observed that the modulus decreased sharply at large N, which is not consistent with our results or with those of Patel et al.; the sharp decrease has been ascribed[27] to the presence of network imperfections. The intercept on the y-axis of Figure 13 should yield the value of G_N^0 from eq 32. Constructing a linear regression fit to the data in Figure 13,[76,64,77] we obtained $G_N^0 = 0.009 \pm 0.002$. If G_N^0 is taken to be equal to the melt plateau modulus from reptation theory,[70] then $G_N^0 = (N_cN/V)(k_BT/N_e)$, and we can calculate the entanglement molecular weight to be $N_e \approx 91$. The squared tube diameter $2\langle R_G^2(N_e)\rangle$ is then $\sim 45\sigma^2$ which is remarkably close to the squared tube diameter of $\sim 40\sigma^2$ obtained from our cross-link MSD study.

The Duering et al. analysis of their network moduli followed a somewhat different procedure. The elastic network moduli from their study also exceeded the affine and phantom moduli at all chain lengths; they ascribed the large moduli to a combination of excluded-volume and entanglement effects and suggested that the simulation moduli be multiplied by a prefactor $A^0 < 1$ in order to account for the excluded-volume effects. They suggested a prefactor value of $^2/_3$ for Lennard-Jones chains, based on their results from a different study.[78] To study entanglement effects, the asymptotic network moduli were displayed in the form $(G_e/x_{\mathrm{elastic}})$ versus $1/N$. They found that the data adhered to a $1/N$ form for intermediate to large N but showed a strong deviation from this for small N ($N < 25$). When the excluded-volume prefactor was not used, the extrapolated y-intercept modulus value yielded an entanglement length that was fairly close to the melt entanglement length. When the prefactor was used, the intercept yielded a value that they called an “effective length”, which was of the order of twice the melt entanglement length. They suggested that the magnitude of the “effective length” signified that about two entanglement lengths were needed to form one effective cross-link.

Holzl et al.[46] recently published bond fluctuation Monte Carlo studies of polymer network deformation in which tetrafunctional, end-linked networks on a cubic lattice were uniaxially extended at constant volume. They found that the force−deformation relations (and hence the moduli) for these systems lay between the affine and phantom predictions. It is not possible to directly compare our data with their results because of the different methods by which the moduli are calculated in the two studies: Holzl et al. calculated their moduli from uniaxially deformed networks, while we calculate our moduli from the chain trajectories of undeformed networks. The moduli from the two methods are expected to yield the same scaling with molecular weight.

Conclusion

Investigations of network dynamics are complicated by a variety of factors that affect network structure and properties: the packing fraction at the time of cross-linking and the method of cross-linking, the packing fraction at which the systems are studied, the molecular weight of the chains, the functionality of the junctions, the fraction and type of network defects, and the contribution of topological constraints. The use of near-perfect end-linked networks with a very small fraction of defects allowed us to greatly reduce the number of variables affecting the network structure, so that we have been able to selectively investigate the effects of molecular weight, packing fraction at the time of cross-linking, functionality, and topological constraints on network behavior.

Our studies explore the nature of the link between the method of network preparation and the network structure and properties. We found that networks constructed at low packing fractions are less interpenetrated and have fewer entanglements than networks constructed at high packing fractions. As a result, the junctions and chains in the low initial density networks have greater freedom of motion than those in high initial density networks. An interesting path of future study would be a systematic investigation of the structure and properties of networks initially cross-linked at a range of packing fractions with a view to obtaining a quantitative relation from simulation, between initial cross-linking density and network behavior.

Our investigation of the network structure showed that the average distance between cross-links is much lower than the average end-to-end distance of a network chain, suggesting that networks are highly interpenetrated and that entanglement effects would be expected to play a very important role in network dynamics. In our study of cross-link and chain dynamics, we found that, at long times, due to the cross-linked nature of the network, the cross-links and chains have a maximum asymptotic mean-squared displacement from their original positions, indicating that they are spatially localized. For short-chain networks, we found that the extent of localization (represented by the asymptotic displacement) is dependent on the network chain length as predicted by the phantom model, while for long-chain networks, the additional constraining effect of chain entanglements causes the extent of localization to be relatively independent of chain length. The comparison of the cross-link asymptotic displacement simulation results with the predictions of the constrained junction model and the Vilgis and Boue localization model suggests that the latter is somewhat more sucessful in predicting the observed trend. However, simulations of longer chain systems than have hitherto been investigated are necessary to confirm our observations.

All the network relaxation moduli exceed the affine model predictions. The molecular weight dependence of the modulus is consistent with experimental observations; at short chain lengths, the modulus appears to be inversely proportional to the molecular weight, while at large chain lengths, the modulus is relatively independent of the molecular weight.

Acknowledgment. This was supported by the GAANN Computational Sciences Fellowship of the U.S. Department of Education, and the Office of Energy Research, U.S. Department of Energy under Contract DE-FG05-91ER14181. We thank the North Carolina Supercomputing Center for grants of CPU time on the Cray Y-MP and T90, and on the workstation cluster.

References and Notes

(1) Wall, F. T. *J. Chem. Phys.* **1943**, *11*, 527.
(2) Flory, P. J. *Principles of Polymer Chemistry*; Cornell U.P.: Ithaca, NY, 1953.
(3) James, H. M.; Guth, E. *J. Chem. Phys.* **1947**, *15*, 669.
(4) Flory, P. J. *Br. Polym. J.* **1985**, *17* (2), 96.
(5) Mark, J. E.; Erman, B. *Rubberlike Elasticity: A Molecular Primer*; Wiley-Interscience: New York, 1988.
(6) Gottlieb, M.; Gaylord, R. J. *Polymer* **1983**, *24*, 1644.
(7) Gottlieb, M.; Gaylord, R. J. *Macromolecules* **1984**, *17*, 2024.
(8) Flory, P. J.; Erman, B. *Macromolecules* **1982**, *15*, 800.
(9) Ronca, G.; Allegra, G. *J. Chem. Phys.* **1975**, *63*, 4990.
(10) Marrucci, G. *Rheol. Acta* **1979**, *18* (2), 193.
(11) Ball, R. C.; Doi, M.; Edwards, S. F.; Warner, M. *Polymer* **1981**, *22*, 1010.
(12) Edwards, S. F.; Vilgis, T. A. *Rep. Prog. Phys.* **1988**, *51*, 243.
(13) Higgs, P. G.; Ball, R. C. *Europhys. Lett.* **1989**, *8* (4), 357.
(14) Adolf, D. *Macromolecules* **1988**, *21*, 228.
(15) Kosc, M. *Colloid Polym. Sci.* **1988**, *266*, 266.
(16) Marrucci, G. *Macromolecules* **1981**, *14*, 434.
(17) Graessley, W. W. *Adv. Polym. Sci.* **1982**, *47*, 68.
(18) Edwards, S. F. *Br. Polym. J.* **1985**, *17*, 123.
(19) Gaylord, R. J. *Polym. Bull.* **1982**, *8*, 325.
(20) Gaylord, R. J.; Douglas, J. F. *Polym. Bull.* **1987**, *18*, 347.
(21) Deam, R. T.; Edwards, S. F. *Philos. Trans. R. Soc. London A* **1976**, *280*, 317.
(22) Goldbart, P.; Goldenfeld, N. *Phys. Rev. Lett.* **1989**, *39* (3), 1412.
(23) Sharaf, M. A.; Mark, J. E.; Alshamsi, A. S. *Polym. J.* **1996**, *28* (5), 375.
(24) Sharaf, M. A.; Mark, J. E. *Polymer* **1994**, *35* (4), 740.
(25) Sung, P. H.; Mark, J. E. *Polym. J.* **1980**, *12* (11), 835.
(26) Rennar, N.; Opperman, W. *Colloid Polym. Sci.* **1992**, *270*, 527.
(27) Patel, S. K.; Malone, S.; Cohen, C.; Gillmor, J. R.; Colby, R. H. *Macromolecules* **1992**, *25*, 5241.
(28) Leung, Y.-K.; Eichinger, B. E. *J. Chem. Phys.* **1984**, *80*, 3877.
(29) Leung, Y.-K.; Eichinger, B. E. *J. Chem. Phys.* **1984**, *80*, 3885.
(30) Shy, L. Y.; Eichinger, B. E. *J. Chem. Phys.* **1989**, *90*, 5179.
(31) Akgiray, O. *Makromol. Chem., Macromol. Symp.* **1993**, *76*, 211.
(32) Gao, J.; Weiner, J. H. *Macromolecules* **1987**, *20*, 2520.
(33) Gao, J.; Weiner, J. H. *Macromolecules* **1987**, *20*, 2525.
(34) Weiner, J. H.; Gao, J. In *Molecular Basis of Polymer Networks*; Baumgartner, A., Picot, C. E., Eds.; Springer-Verlag: New York, 1989.
(35) Duering, E. R.; Kremer, K.; Grest, G. *Phys. Rev. Lett.* **1991**, *67*, 3531.
(36) Duering, E. R.; Kremer, K.; Grest, G. *Prog. Colloid Polym. Sci.* **1992**, *90*, 13.
(37) Grest, G. S.; Kremer, K.; Duering, E. R. *Physica A* **1993**, *194*, 330.
(38) Duering, E. R.; Kremer, K.; Grest, G. *J. Chem. Phys.* **1994**, *101*, 8169.
(39) Vilgis, T. A.; Boue, F. *J. Polym. Sci.: Polym. Phys.* **1988**, *26*, 2291.
(40) Vilgis, T. A. In *Elastomeric Polymer Networks*; Mark, J. E., Erman, B., Eds.; Prentice-Hall: Englewood Cliffs, NJ, 1992.
(41) Kremer, K.; Grest, G. S. *J. Chem. Phys.* **1990**, *92*, 5057.
(42) Langley, N. R. *Macromolecules* **1968**, *1*, 348.
(43) Pearson, D. S.; Graessley, W. W. *Macromolecules* **1978**, *11*, 528.
(44) Dossin, L. M.; Graessley, W. W. *Macromolecules* **1979**, *12*, 123.
(45) Trautenberg, H. L.; Sommer, J. U.; Goritz, D. *J. Chem. Soc., Faraday Trans.* **1995**, *91*, 2649.
(46) Holzl, T.; Trautenberg, H. L.; Goritz, D. *Phys. Rev. Lett.* **1997**, *79*, 2293.
(47) Escobedo, F. A.; de Pablo, J. J. *J. Chem. Phys.* **1996**, *104*, 4788.
(48) Escobedo, F. A.; de Pablo, J. J. *J. Chem. Phys.* **1997**, *106*, 793.
(49) Escobedo, F. A.; de Pablo, J. J. *J. Mol. Phys.* **1997**, *90*, 437.
(50) Mark, J. E. In *Physical Properties of Polymers*, 2nd ed.; Mark, J. E., Eisenberg, A., Graessley, W. W., Mandelkern, L., Samulski, E. T., Koenig, J. L., Wignall, G. D., Eds.; American Chemical Society: Washington DC, 1993.

(51) Brotzman, R. W.; Eichinger, B. E. *Macromolecules* **1981**, *14*, 1445.
(52) Urayama, K.; Kohjiya, S. *J. Chem. Phys.* **1996**, *104*, 3352.
(53) de Gennes, P. G. *Scaling Concepts in Polymer Physics*; Cornell U.P.: Ithaca, NY, 1979.
(54) Rapaport, D. C. *J. Phys. A.: Math. Gen.* **1978**, *11*, L213.
(55) Rapaport, D. C. *J. Chem. Phys.* **1979**, *71*, 3299.
(56) Bellemans, A.; Orban, J.; Belle, D. V. *Mol. Phys.* **1980**, *39*, 781.
(57) Alder, B. J.; Wainwright, T. E. In *International Symposium on Transport Processes In Statistical Mechanics*; Prigogine, I., Ed.; Interscience: New York, 1956.
(58) Alder, B. J.; Wainwright, T. E. *J. Chem. Phys.* **1959**, *31*, 459.
(59) Haile, J. M. *Molecular Dynamics Simulation: Elementary Methods*; Wiley: New York, 1992.
(60) Alder, B. J.; Wainwright, T. E. *J. Chem. Phys.* **1960**, *33*, 1439.
(61) Smith, S. W.; Freeman, B. D.; Hall, C. K. *J. Comput. Phys.* **1997**, *134*, 16.
(62) Smith, S. W.; Freeman, B. D.; Hall, C. K. *J. Chem. Phys.* **1996**, *104*, 5616.
(63) Scanlan, J. *J. Polym. Sci.* **1960**, *43*, 501.
(64) Pearson, D. S.; Graessley, W. W. *Macromolecules* **1977**, *11*, 528.
(65) Ferry, J. D. *Viscoelastic Properties of Polymers*; Wiley: New York, 1980.
(66) McQuarrie, D. A. *Statistical Mechanics*; Harper and Row: New York, 1973.
(67) Erman, B.; Flory, P. J. *Macromolecules* **1982**, *15*, 806.
(68) Fetters, L. J.; Lohse, D. J.; Richter, D.; Witten, T. A.; Zirkel, A. *Macromolecules* **1994**, *27*, 4639.
(69) Vilgis, T. A.; Boue, F. *Polymer* **1986**, *27*, 71.
(70) Doi, M.; Edwards, S. F. *The Theory of Polymer Dynamics*; Clarendon: Oxford, 1986.
(71) Obukhov, S. P.; Rubinstein, M.; Colby, R. H. *Macromolecules* **1994**, *27*, 3191.
(72) Vilgis, T. A.; Heinrich, G. *Phys. Rev. E* **1994**, *49*, 2167.
(73) Ewen, B.; Richter, D. In *Elastomeric Polymer Networks*; Mark, J. E., Erman, B., Eds.; Prentice-Hall: Englewood Cliffs, NJ, 1992.
(74) de Gennes, P. G. *J. Phys.* **1981**, *42*, 735.
(75) Heinrich, G.; Straube, E.; Helmis, G. *Adv. Polym. Sci.* **1988**, *85*, 33.
(76) Dossin, L. M.; Graessley, W. W. *Macromolecules* **1979**, *12*, 123.
(77) Gottlieb, M.; Macosko, C. W.; Benjamin, G. S.; Meyers, K. O.; Merrill, E. W. *Macromolecules* **1981**, *14*, 1039.
(78) Everaers, R.; Kremer, K. *Macromolecules* **1995**, *28*, 7291.

MA9801422